NORWEGIAN JOURNAL OF GEOLOGY
https://dx.doi.org/10.17850/njg100-1-2

GEOLOGICAL SOCIETY OF NORWAY

Late Palaeozoic fault-controlled hydrothermal Cu–Zn mineralisation on Vanna island, West Troms Basement Complex, northern Norway

Hanne-Kristin Paulsen[1,2], Steffen G. Bergh[1] & Sabina Strmić Palinkaš[1]

[1]University of Tromsø (UiT),The Arctic University of Norway, 9037 Tromsø, Norway.
[2]Present address: Geological Survey of Norway, 7491 Trondheim, Norway.

E-mail corresponding author (Hanne-Kristin Paulsen): hanne-kristin.paulsen@ngu.no

Keywords:
· Epigenetic mineralisation
· Post-Caledonian brittle fault
· Fluid inclusions
· Stable isotopes
· Incipient continental rifting
· Cataclasite zone

Received 26. April 2019
Accepted 7. January 2020
Published online 31. March 2020

The Vannareid–Burøysund fault is a major, brittle, normal fault in northern Norway, with cohesive fault rocks (cataclasites) that host Cu–Zn-bearing quartz-carbonate veins. The fault is exposed on the island of Vanna in the Neoarchaean to Palaeoproterozoic West Troms Basement Complex, separating variably deformed tonalitic gneisses in the footwall from mylonitised metasedimentary rocks and tonalites in the hanging wall. Radiometric dating (K–Ar illite) of normal fault movement along the Vannareid–Burøysund fault yielded a late Permian age, concurrent with incipient post-Caledonian continental rifting. The fault evolution and internal architecture of the Vannareid–Burøysund fault largely controlled the spatial distribution of mineralisation, and two main phases of the Cu–Zn mineralisation have been discerned. Early quartz-sphalerite veins are deposited in the cataclastic fault core zone, where initial movement along the fault created a fluid conduit that allowed for fluid flow and sphalerite deposition. With subsequent movement and widening of the fault zone, a later and spatially more extensive generation of quartz-chalcopyrite veins were deposited in both the fault core and the damage zones. Fluid inclusion micro-thermometry revealed that the ore-forming fluids were highly saline aqueous solutions (20–37 wt.% NaCl + $CaCl_2$) that carried base metals and sulphur. Further, the isotopic composition of hydrothermal carbonates indicates a magmatic source for the CO_2. The structural data and obtained geochemical results indicate that the Cu–Zn mineralisation in the Vannareid–Burøysund fault was epigenetic and strongly controlled by extensional brittle faulting and cataclasis during early stages of post-Caledonian (Permian) continental rifting, thus providing a new model for exploration of post-Caledonian hydrothermal ore deposits in basement rocks of northern Norway.

Introduction

Cu–Zn mineralisation is found in a variety of geological settings, such as volcanogenic massive sulphide (VMS) deposits (Franklin et al., 1981; Galley et al., 2007), skarn deposits (Meinert et al., 2005), black shale hosted Cu–Zn deposits (Kupferschiefer; Kucha & Pawlikoswki, 1986; Oszczepalski, 1999), sediment hosted Cu–Zn deposits (Perelló et al., 2015), and hydrothermal vein deposits (Corbett & Leach, 1998; Simmons et al., 2005).

© Copyright the authors.
This work is licensed under a Creative Commons Attribution 4.0 International License.

Paulsen, H.K., Bergh, S.G. & Palinkaš, S.S. 2020: Late Palaeozoic fault-controlled hydrothermal Cu–Zn mineralisation on Vanna island, West Troms Basement Complex, northern Norway. *Norwegian Journal of Geology 100*, 1–41. https://dx.doi.org/10.17850/njg100-1-2.

Key factors that may control the deposition of significant Cu–Zn mineralisation include a source of metals (Rye & Ohmoto, 1974; Boiron et al., 2010), an aqueous fluid capable of transporting metal complexes (Hemley & Cygan, 1992; Zhong et al., 2015), rock permeability that allows fluid flow (Sibson et al., 1975; Ingebritsen & Manning, 2010), and favourable physicochemical conditions for Cu and Zn deposition (Seward & Barnes, 1997; Vaughan & Craig, 1997; Corbett & Leach, 1998). In crystalline rocks in the upper crust, brittle faults and fracture systems represent important conduits for ore-bearing fluids in otherwise non-permeable rocks (Sibson, 1977; Wise et al., 1984; Schmid & Handy, 1991; Braathen & Davidsen, 2000; Gabrielsen & Braathen, 2014).

In this study, we analysed a major brittle normal fault in northern Norway, the Late Palaeozoic/Permian Vannareid–Burøysund fault (VBF), and its cohesive brittle fault rocks (cataclasites) hosting Cu–Zn-bearing quartz-carbonate veins. The fault is situated along the contact between Neoarchaean tonalitic basement gneisses and an overlying, mixed basement and metasedimentary thrust unit, the Skipsfjord Nappe (Opheim & Andresen, 1989; Monsen, 2014). The Cu–Zn mineralisation was discovered in 2008 and briefly explored in 2012 when an exploration company (Store Norske Gull) drilled totalling a length of 880 m, and informally interpreted the mineralised occurrence as a Palaeoproterozoic VMS type (Ojala et al., 2013). Follow-up studies showed Cu–Zn and sulphide enrichment in vein and brecciated/cataclastic fault rocks indicating extensive hydrothermal alteration (Monsen, 2014). This paper expands the goals to explore ore-forming processes based on fault-rock architectures, ore-hosting vein and host-rock mineral geochemistry, fluid inclusion microthermometry and decrepitation studies, and stable isotope data.

These goals are achieved by studying the brittle fault zone architecture (domains in section across the fault) and meso- and microscale textures of the resulting fault rocks in relation to ore-hosting hydrothermal quartz-carbonate veins. The mineralogical and geochemical changes of the host rock during infiltration of ore-bearing fluids and the mineralisation process have been studied in detail. In addition, P-T-X conditions estimated by use of microthermometric data obtained from fluid inclusions in quartz, sphalerite and calcite in hydrothermal veins are discussed. These data are also used to calculate the fluid composition in order to discuss metal mobility and depositional mechanisms of mineralisation relative to the brittle faulting events. Fluid compositions and stable isotope geochemistry of carbonates are used to infer potential sources of the Cu–Zn-bearing hydrothermal fluids.

Geological setting

Vanna is a coastal island located in the Neoarchaean–Palaeoproterozoic West Troms Basement Complex (WTBC) in northern Norway (Fig. 1; Bergh et al., 2010). This basement province is located west of, and structurally below, the much younger Palaeozoic Caledonian thrust nappes (Augland et al., 2014; Roberts & Lippard, 2005), which to the east are down-faulted several km by the regional Vestfjord–Vanna Fault Complex (Fig. 1; Olesen et al., 1997; Indrevær et al., 2013). The WTBC (Fig. 2) is composed of segmented crustal blocks of tonalitic, trondhjemitic to granitic gneisses (2.9–2.6 Ga) overlain by supracrustal units (2.8 –1.9 Ga; Armitage & Bergh, 2005; Myhre et al., 2011, 2013), and intruded by felsic and mafic igneous rocks (c. 1.8 Ga; Corfu et al., 2003; Bergh et al., 2010). In the north of the WTBC, on the islands of Ringvassøy and Vanna, mafic dyke swarms (2.4 Ga) intruded the basement gneisses (Kullerud et al., 2006).

In southern parts of Vanna (Fig. 3), a parautochthonous metasedimentary sequence, the Vanna Group, unconformably overlies the basement gneisses (Binns et al., 1980; Johansen, 1987). Its age is constrained by the older 2.4 Ga dykes present below the unconformity, and an intrusive diorite sill in the metasedimentary rocks dated at 2.2 Ga (Bergh et al., 2007). The Vanna Group metasedimentary rocks are composed of arkosic, shallow deltaic sandstones and calcareous mud- and siltstones (Binns et al., 1980; Johannessen, 2012). These cover units and the tonalitic basement in Vanna were all affected by contractional deformation and low-grade metamorphism (greenschist facies) during the Svecofennian orogeny (c. 1.8–1.77 Ga) and/or during younger Caledonian tectonothermal events (Dallmeyer, 1992; Bergh et al., 2007, 2010; Myhre et al., 2013). The Svecofennian event produced a foreland fold and thrust

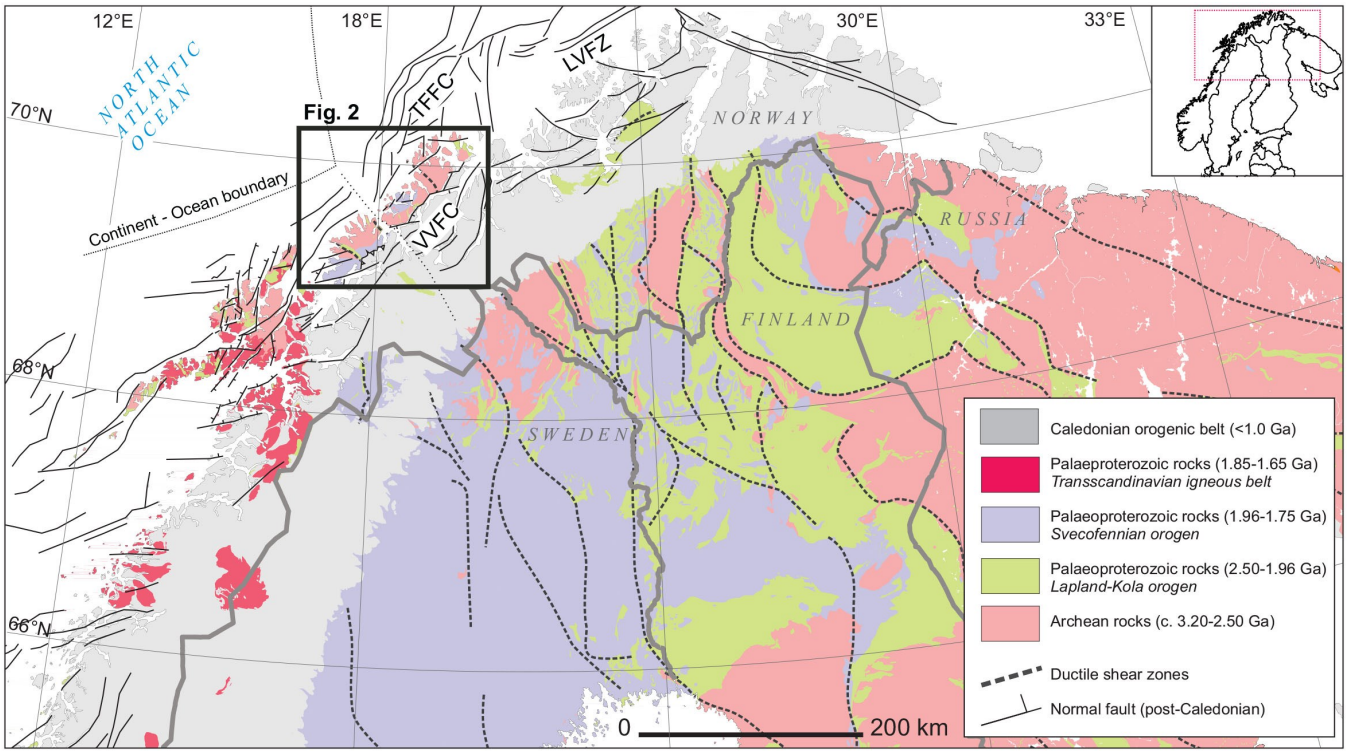

Figure 1. Regional geological map of the northern Fennoscandian Shield (based on Koistinen et al., 2001; Olesen et al., 2002; Eilu et al., 2008; Bergh et al., 2010; Davids et al., 2013; Koehl et al., 2018b). For the main legend, see Koistinen et al. 2001. The black frame outlines the West Troms Basement Complex (Fig. 2), a basement horst controlled by the onshore Vestfjorden–Vanna Fault Complex (VVFC) that down-faults the Caledonian rocks to the east. This Permian–Early Triassic rift-related activity can also be correlated with offshore fault systems including the Troms–Finnmark Fault Complex (TFFC) and the Langfjorden–Vargsundet fault zone (LVFZ).

belt in Vanna (Bergh et al., 2007), which in the northern part of the island included the Skipsfjord Nappe (Binns et al., 1980; Opheim & Andresen, 1989; Rice, 1990). The Skipsfjord Nappe consists of repeated thrust sequences of locally highly strained and mylonitised basement tonalites, alternating with lenses/ sheets of relict Vanna Group metasedimentary rocks, and sheared mafic and felsic intrusive rocks. Its thrust contact to autochthonous gneisses is exposed in the south at Skipsfjorden and Slettnes (Fig. 3).

In the northern part of Vanna island (Fig. 3), the Skipsfjord Nappe is down-faulted in the hanging wall by the VBF (Bergh et al., 2007; Opheim & Andresen, 1989). This fault is a splay fault to the regional, ENE–WSW-trending, zigzag-shaped, Vestfjord–Vanna Fault Complex (Fig. 2) that bounds the WTBC horst against Caledonian nappes to the east (Forslund, 1988; Olesen et al., 1997; Indrevær et al., 2013, 2014). Offshore to the northwest, the WTBC horst abuts against the Troms–Finnmark Fault Complex (Indrevær et al., 2013) (Figs. 1 & 2). The WTBC horst and its bounding normal faults all formed during incipient rifting of the North Atlantic Ocean in the Early Permian–Triassic (Fig. 1; Blystad et al., 1995; Mosar et al., 2002; Faleide et al., 2008; Davids et al., 2013, 2018; Gabrielsen & Braathen, 2014; Koehl et al., 2018a, b), and this rifting event affected the entire North-Norwegian passive continental margin (Mosar, 2003).

The present study focuses on a mineralised segment (Fig. 4) of the VBF (Opheim & Andresen, 1989) that hosts Cu–Zn mineralisation. The VBF is a brittle oblique-normal fault striking ENE–WSW and dipping c. 50–60° to the SSE. It separates variably deformed Neoarchaean tonalitic gneisses intruded by mafic dykes (2.2 –2.4 Ga), diorite and gabbro, in the footwall from mylonitised tonalites and metasedimentary rocks of the Skipsfjord Nappe in the hanging wall, with a minimum vertical throw in the order of 2–3 km (Opheim & Andresen, 1989). A section through the VBF shows a <100 m-wide fault complex including fault gouge core

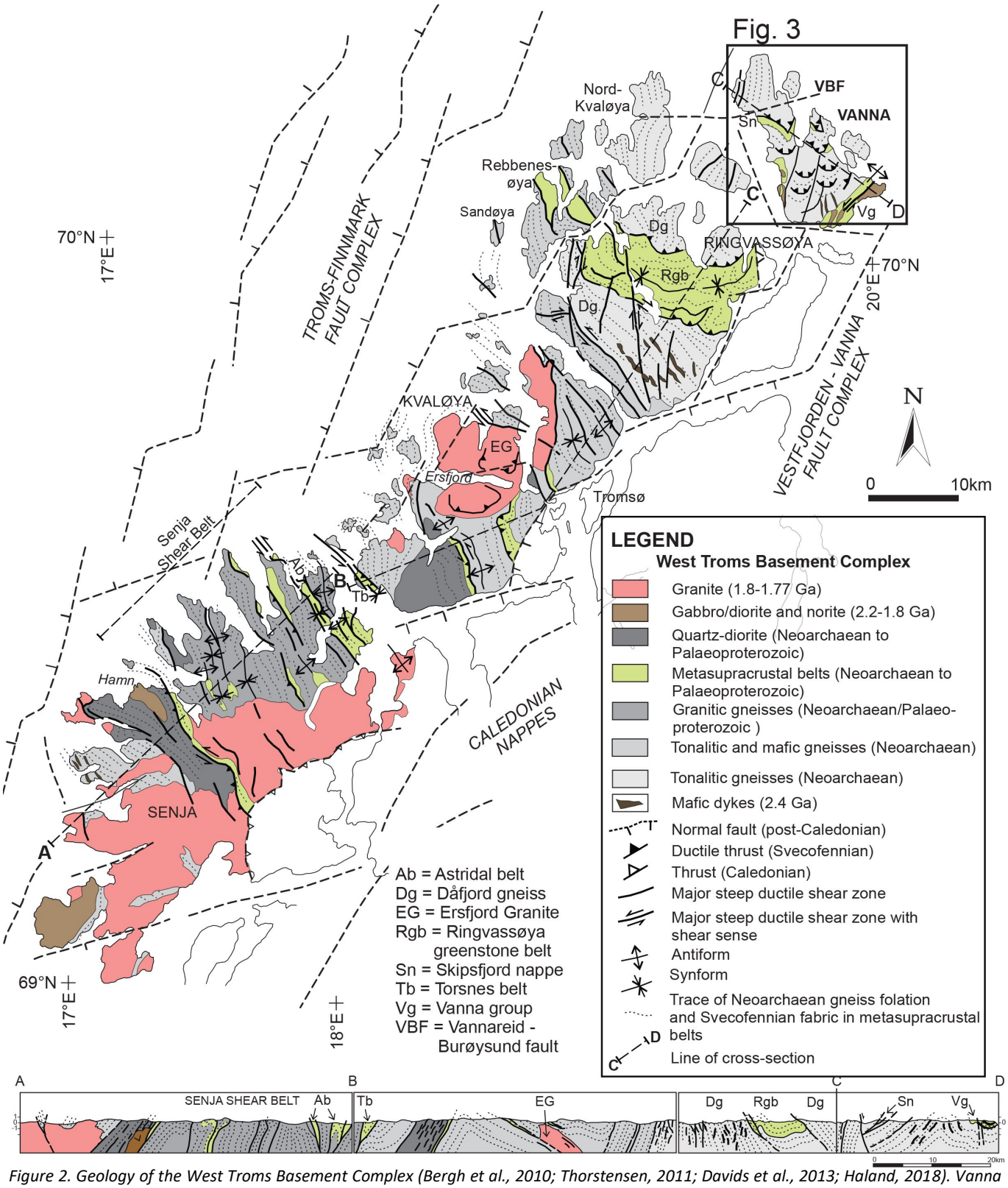

Figure 2. Geology of the West Troms Basement Complex (Bergh et al., 2010; Thorstensen, 2011; Davids et al., 2013; Haland, 2018). Vanna island is located at the northern end of the complex. The location of the mineralised Vannareid–Burøysund fault (VBF) is marked on the map. The VBF is part of the Vestfjorden–Vanna and Troms–Finnmark fault complexes offshore and along fjords and sounds. The black frame outlines the island of Vanna (Fig. 3).

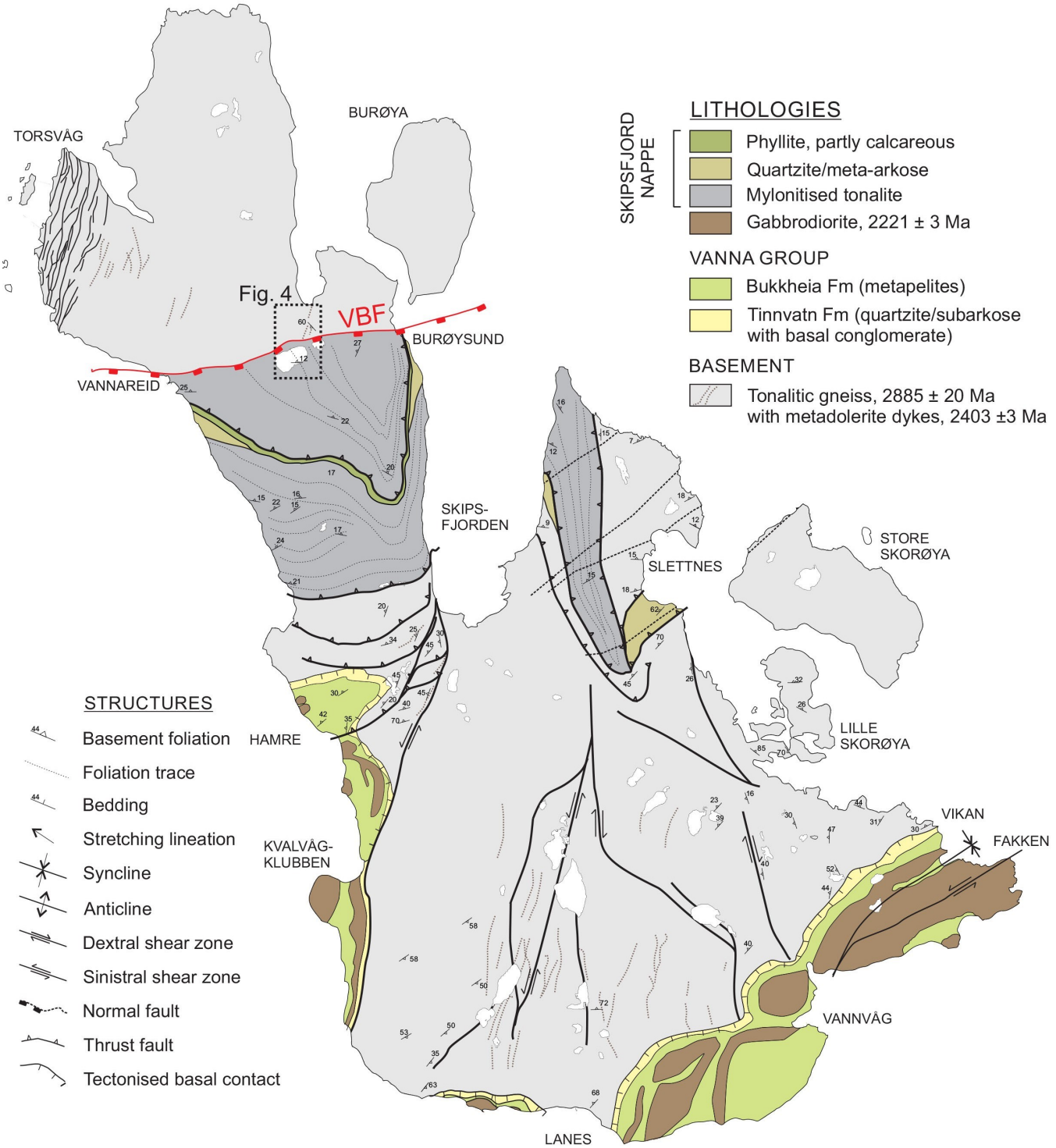

Figure 3. Geological map of Vanna (Bergh et al., 2007). The mineralised Vannareid–Burøysund fault (VBF) separates variably deformed tonalite gneiss to the north from highly strained and mylonitised Skipsfjord Nappe rocks to the south. The small black frame outlines the mineralised segment of the VBF (Fig. 4).

and damage zones. K–Ar illite dating and $^{40}Ar/^{39}Ar$ dating of K-feldspar in the fault gouge core yielded Late Carboniferous (348.5 Ma) through Early Permian (283.9 Ma) ages (Davids et al., 2013, 2018), concurrent with known periods of incipient rift-margin extensional faulting and associated fluid infiltration and reactivation (Indrevær et al., 2014; Davids et al., 2018).

We analysed the VBF and its mineralised sections, and attempted to resolve its role as a pathway for hydrothermal fluids and the conditions that caused ore mineral dposition along the VBF. The results may have important implications for understanding ore genesis and for exploration purposes of Cu–Zn deposits in northern Norway.

Methodology

Fieldwork and drillcore data

Fieldwork (c. five days) and structural analysis of the VBF focussed on characterisation of the fault core and damage zones surrounding the mineralised fault segment and adjacent host rocks. These studies were combined with four days of detailed core logging of c. 880 m of non-oriented drillcores drilled by Store Norske Gull (SNG) in 2012, to identify and describe fault rocks, fabric domains, and cross-cutting relationships of fabrics and hydrothermal veins. Sixty-one drillcore samples and five outcrop rock samples were collected from the VBF core zones, damage zones, hydrothermal mineralised veins, and the surrounding host rocks. Microtextural analysis of polished thin-sections was undertaken using conventional transmitted and reflected light microscopy. We used an existing dataset obtained by SNG of 783 drillcore assays (0.15–2 m sample length) of host rocks, fault rocks, and mineralised hydrothermal veins analysed by ALS-Geochemistry Analytical Lab. This dataset contains analyses of whole rock geochemistry (analysed fused pellets using XRF) and a 48-element suite (analysed using four-acid digest and ICP-MS finish). Samples with ore grade Zn and Cu (>10,000 ppm) were re-analysed using sodium peroxide fusion with an ICP-AES finish.

Scanning electron microscope data

Scanning electron microscope (SEM) analysis including energy-dispersive X-ray spectroscopy (EDS), electron backscattered diffraction (EBSD), and cathodo-luminescence (CL), was used to determine mineral chemistry, mineral parageneses, mineralogical changes, e.g., zonation in hydrothermal quartz, and textural relationships. The thin-sections were coated with a thin carbon layer to avoid charging effects. All the analyses were carried out using a Zeiss Merlin VP Compact field emission SEM equipped with an X-max^{80} EDS detector and a Nordlys EBSD detector, both provided by Oxford Instruments, as well as a Zeiss variable pressure secondary electron (VPSE) detector for CL imaging. The VPSE detector uses the CL signal and produces an image close to panchromatic CL under high vacuum conditions (Griffin et al., 2010). EDS measurements were done at 20 kV acceleration voltage and a 60 µm aperture size. For EBSD, the sample was tilted to 70 degrees; 20 kV acceleration voltage and a 240 µm aperture was applied. A step-size of 5 µm was chosen for EBSD mapping and a minimum number of 6 detection bands was applied for indexing. The AZtec software by Oxford Instruments was used for data acquisition and further post-processing of the EDS and EBSD data. Backscatter images (BSE) were acquired under the same conditions as EDS measurements. For VPSE imaging, an acceleration voltage of 20 kV was applied as well as an aperture of 120 µm. The vacuum conditions were higher than 1×10^{-5} mbar within the sample chamber. EDS chemical analysis of chlorite in fault rocks was used to estimate formation temperatures based on tetrahedral site occupancy (Cathelineau, 1988), which is accurate to within 30°C. EDS measurements were standardised using a cobalt standard.

X-ray diffraction data

X-ray diffraction (XRD) analyses were performed on consolidated fault rocks (cataclasites) to determine mineralogy of very fine-grained samples. The analyses were conducted at the University of Zagreb on a Philips PW 3040/60 X'Pert PRO powder diffractometer (45 kV, 40 µA), with CuKα-monochromatised radiation (λ = 1.54056 Å) and θ–θ geometry. The area between 4 and 63° 2θ, with 0.02° steps, was measured with a 0.5° primary beam divergence. Compound identificatins were based on a computer program X'Pert high score 1.0B and literature data.

Fluid inclusion data

Fluid inclusion data were obtained from double-polished wafers (100–250 µm thick) of hydrothermal quartz, sphalerite and calcite. Homogenisation temperatures (T_h), halite melting temperatures (T_s), final ice melting temperatures ($T_{m\ Ice}$), and eutectic temperatures (T_e) were recorded using an Olympus BX 2 microscope coupled with a Linkam THMS 600 heating and cooling stage operating between -180 and +600° C at UiT-The Arctic University of Norway. Fluid inclusions were classified according to Roedder (1984) and Sheperd (1985). Salinities of the H_2O–NaCl–$CaCl_2$ system were calculated in NaCl + $CaCl_2$ weight percent using known eutectic temperature as well as halite and ice melting temperatures (Bodnar & Vityk, 1994; Steele-MacInnis et al., 2011). In addition, qualitative measurements of key elements and complexes present in the hydrothermal fluid were obtained by decrepitating fluid inclusions (c. 500°C for 3–4 minutes) and analysing the resulting evaporate mounds formed on the sample surface using a SEM/EDS technique according to the procedure modified after Kontak (2004). We performed both spot analysis of specific mineral phases and a map scan over the whole evaporate mound.

Stable isotope data

We obtained twenty-two $\delta^{13}C$ and $\delta^{18}O$ stable isotope analyses of hydrothermal calcite veins, calcite from host-rock mica schists in the Skipsfjord Nappe hanging wall to the VBF, and calcites from veins and hydrothermal breccia adjacent to an intrusive diorite sill in the Vanna Group farther south (see Fig. 3 for location). These analyses were obtained using a Thermo-Fisher MAT253 IRMS with a Gasbench II at UiT (site.uit.no/sil). Samples were placed in 4.5 ml Labco vials, then flushed with He, and 5 drops of water-free H_3PO_4 were added manually with a syringe. The results were normalised to Vienna Pee Dee Belemnite (VPDB) standard by three in-house standards with a wide range of $\delta^{13}C$ and $\delta^{18}O$ values, and reported with an uncertainty of standard deviation ≤0.1‰.

Results

Fault geometry and textural subdivision

From a regional perspective, the VBF is discernible on ortho-photos and digital elevation maps as an ENE–WSW-trending linear valley between Vannareid and Burøysund on the island of Vanna (Fig. 3). The fault itself is partly exposed in a road section in this valley (Fig. 4), but is otherwise mostly covered by glacial and valley debris. The surrounding basement gneisses in the footwall and metapsammites and schists of the Skipsfjord Nappe in the hanging wall, are however, well exposed along the shores of Vanna both to the east and to the west. Where exposed, splays of the VBF strike ENE–WSW and dip 45–50° to the SSE (Fig. 4; Opheim & Andresen, 1989; Monsen, 2014). The foliation of the quartz-mica schists in the hanging wall of the VBF strikes mostly ENE–WSW and dips gently to the NNW, but adjacent to the VBF the foliation on a

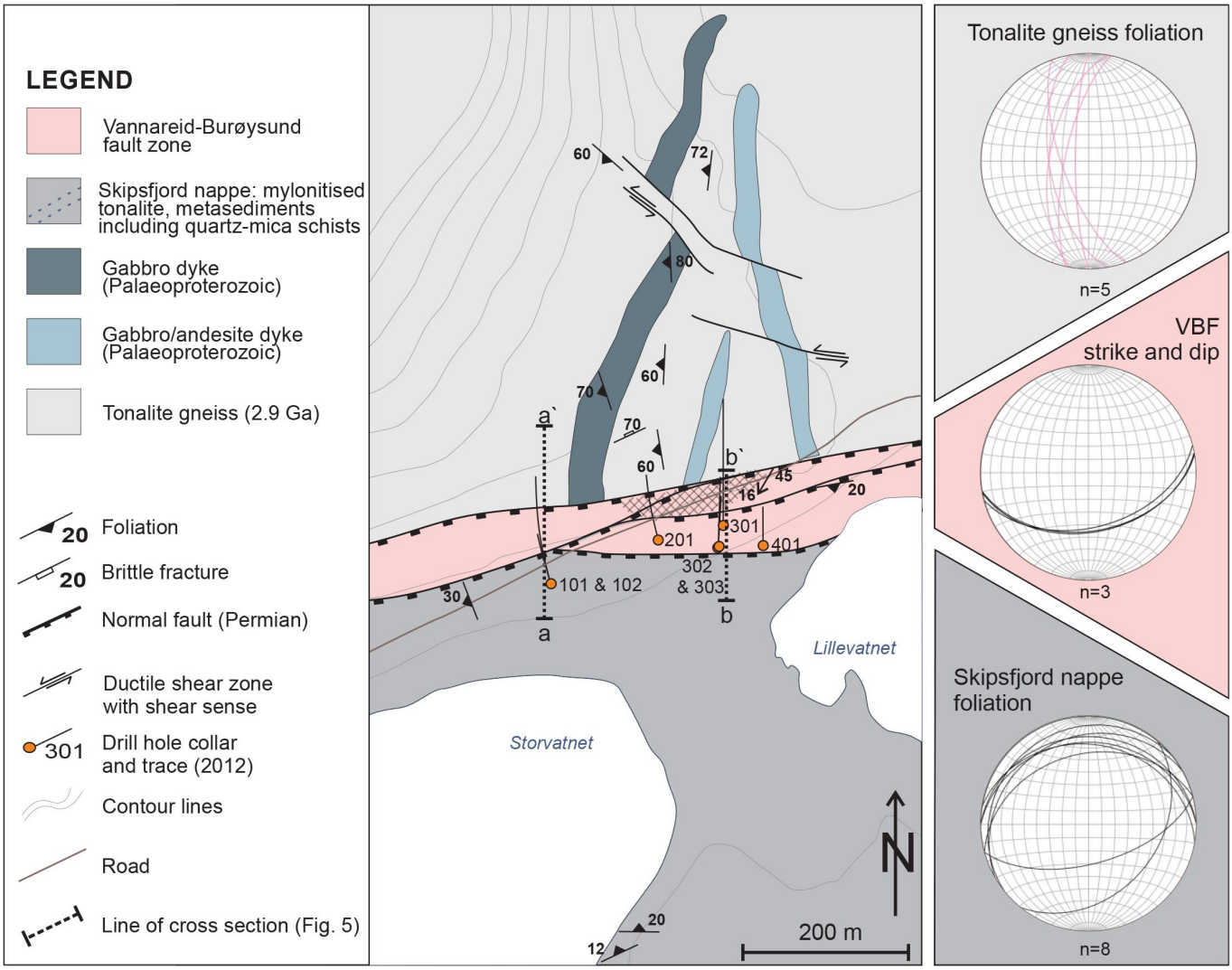

Figure 4. Geological map of the mineralised segment of the VBF in the valley between Vannareid and Burøysund (see Fig. 3 for location), with enclosed fault details to the right outlined as great circles in lower-hemisphere stereoplots. Note several splay faults of the VBF, a gentle NW dip of the foliation in the Skipsfjord Nappe changing to a SE dip close to the VBF. The map is modified after Monsen (2014). Existing drillcore locations are marked on the map (Ojala et al., 2013). Profile lines a-a' and b-b' mark the locations of profiles shown in Fig. 5.

large scale is tilted to a c. 50° dip to the SSE. This change in dip may be due to drag folding caused by normal, down-to-the-SSE movement of the VBF.

This study focuses on the mineralised part of the VBF (Figs. 4 & 5). The surface expression of the fault is a scarp with a c. 10 m-thick core zone that can be followed for c. 25 m along strike. In outcrop, the fault zone is pronounced (Fig. 6A) and made up of pale-green chlorite-rich proto- and ultracataclasite cut by networks of irregular quartz and calcite veins with sphalerite and chalcopyrite (Fig. 6B). Where exposed, the fault surface itself is planar and coated with green-coloured chlorite and epidote (Fig. 6A). A local presence of epidote slickenside fibres indicates normal-oblique, down-to-the-SSE movement along the fault. Combined surface mapping, logged drillcore, and petrographic data show six textural domains across the C. 120 m-thick VBF (Fig. 5). These include two fault core zones (Fig. 5; domains A1 & A2), characterised by various types of cataclastic fault rocks (Figs. 6 & 7), and two damage zones (Fig. 5; domains B1 & B2), with complex internal veins and fracture networks (Figs. 8 & 9). The remaining domains, domain C and domain D, occur in

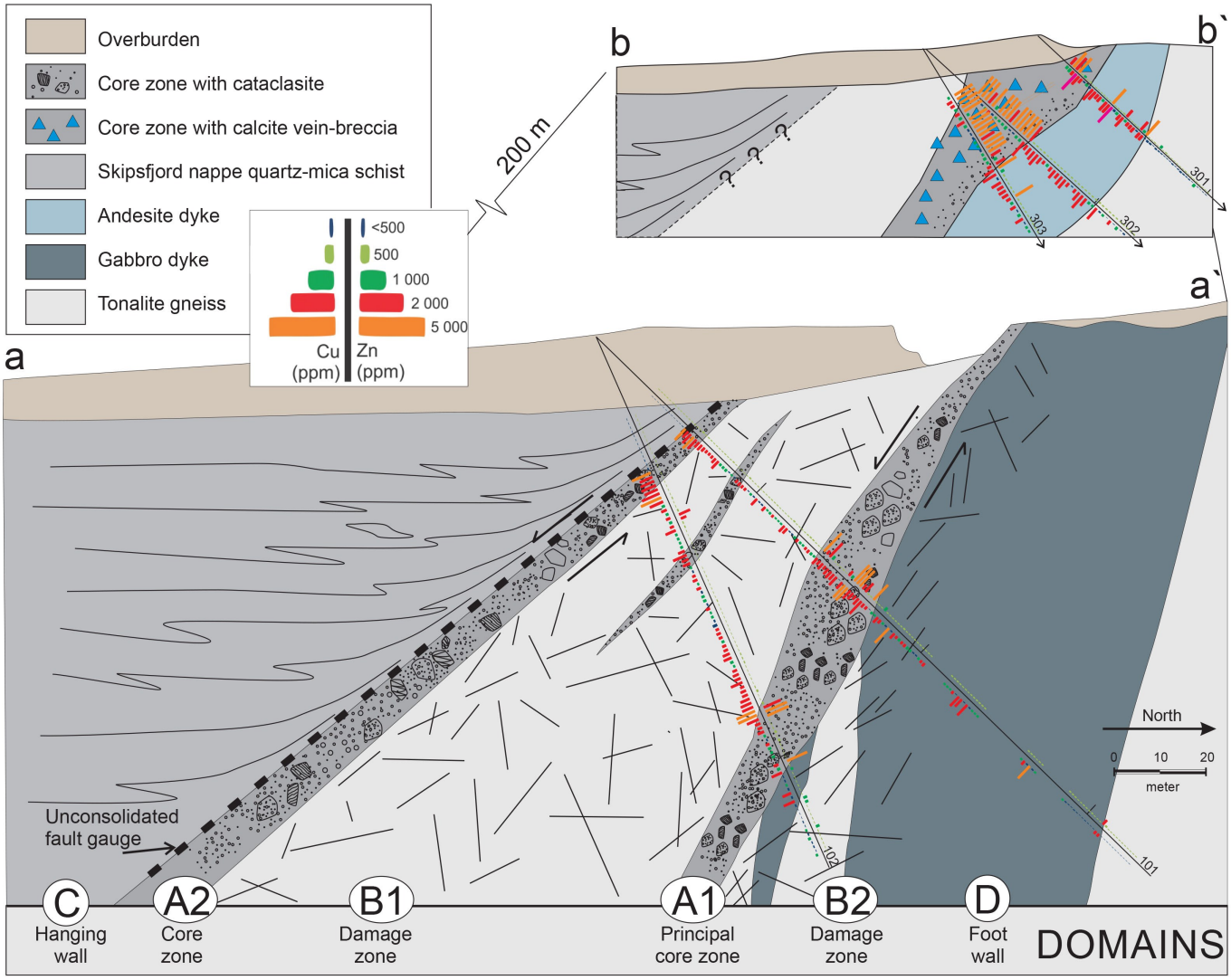

Figure 5. Cross-section a-a' through the VBF showing the two drillcores and interpreted textural domains in mineralised fault rocks (core zone A1 and A2) and surrounding host rocks (damage zones B1 and B2; hanging wall domain C; and footwall domain D). The coloured assay data reflect the amount of Zn (ppm), plotted on the right side of the drillcore, and Cu (ppm) on the left side. Note enrichment of Cu–Zn in core zones A1 and A2, whereas lower values exist in damage zones B1 and B2. The down-dropped, non-deformed, hanging wall rocks of the Skipsfjord Nappe are barren of ore mineralisation. The inset figure in the top right shows cross-section b-b' through the VBF c. 200 m farther east, with thick calcite-breccias making up the fault core zone A1.

the surrounding host rocks of the hanging wall (Fig. 10) and footwall, respectively. Notably, the fracture networks in both core and damage zones contain an extensive number of hydrothermal quartz-calcite veins with pronounced Cu–Zn mineralisation (Fig. 11), described below.

Domain A1 (core zone) is c. 15 m thick and the principal fault core zone located in the footwall, at the contact between host rocks of tonalitic gneiss and a gabbroic dyke. It is characterised by multiple generations of cohesive cataclasites with 20–50% sub-rounded, polymict clasts of tonalite gneiss, older cataclasite, sphalerite, and quartz in a palegreen fine-grained quartz-chlorite matrix (Figs. 7 & 11A). Multiple generations of hydrothermal veins are identified within the cataclasites of domain A1 and make up c. 60% of the material in this core zone (Fig. 11A).

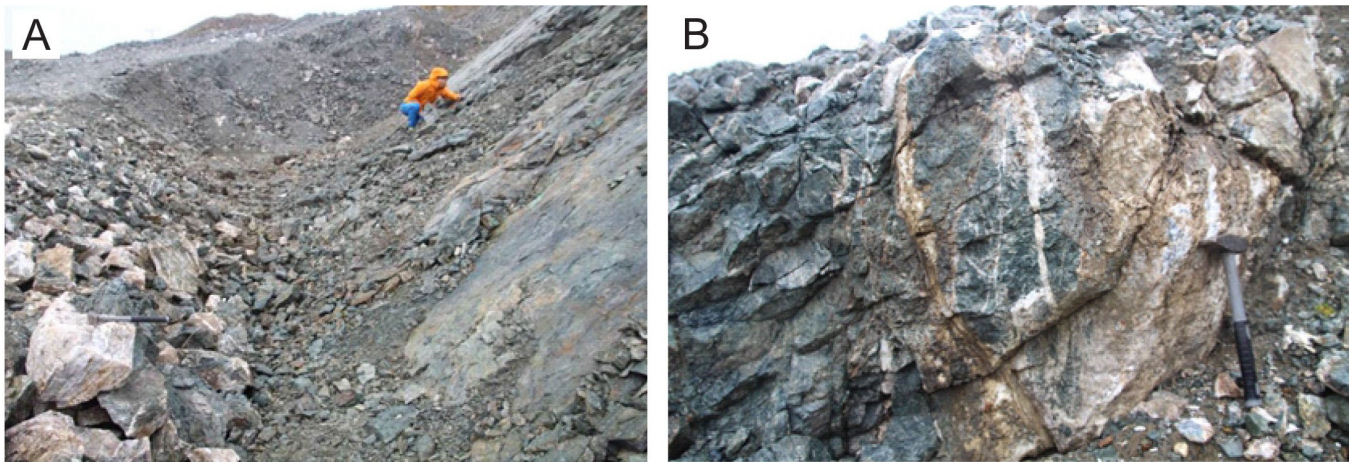

Figure 6. (A) Outcrop photo of the VBF, expressed as a planar, moderately dipping, locally striated surface, with malachite and epidote staining. Person for scale. (B) Outcrop photo of altered/chloritised (green colour) bedrock and protocataclasites in damage zone B1 of the VBF. Note the presence of abundant hydrothermal quartz and calcite veins as infill in brittle fractures.

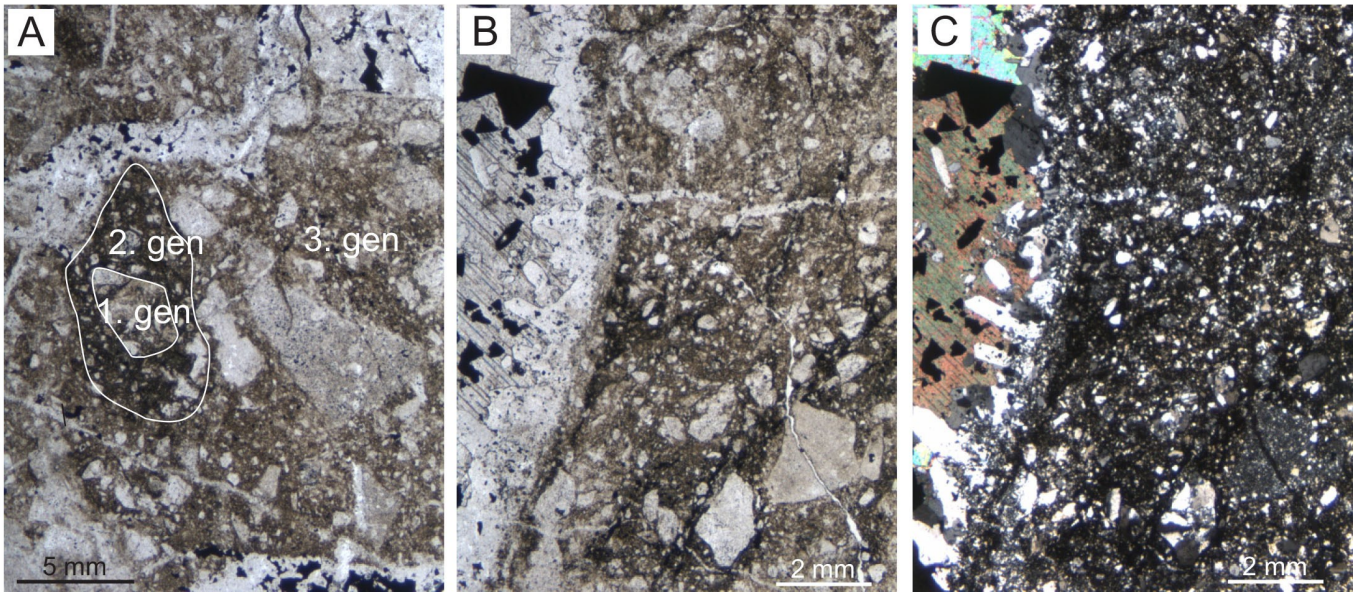

Figure 7. (A) Photomicrograph (PPL) of three generations of cataclasite from core zone A1. These cataclasites are cross-cut by a younger, hydrothermal, chalcopyrite-bearing quartz vein (top right to middle left). (B) Photomicrograph (PPL) from core zone A1 showing details of several generations of cataclasite to the right and hydrothermal quartz-calcite vein to the left that are growing from the consolidated clast (s) of cataclasite. The rims of this vein are composed of euhedral quartz with calcite infill. (C) Same as in B but as XPL.

In thin-section, the cataclasites have a dismembered texture with sub-rounded to rounded, consolidated clasts of at least two generations of fine-grained cataclasite embedded as new clasts within a third generation (Fig. 7A–C). The matrix of all generations of cataclasite is microcrystalline with an internal grain size of 0.1 to 5 mm, and composed of quartz (c. 98%), chlorite, microcline and minor albite and cookeite (based on XRD and SEM analyses). Along strike farther west, the texture and mineralogy of core zone A1 changes and is a c. 15 m-wide complex cataclasite containing decimetre-sized clasts of mainly calcite and sphalerite cemented by calcite veins (Fig. 11B).

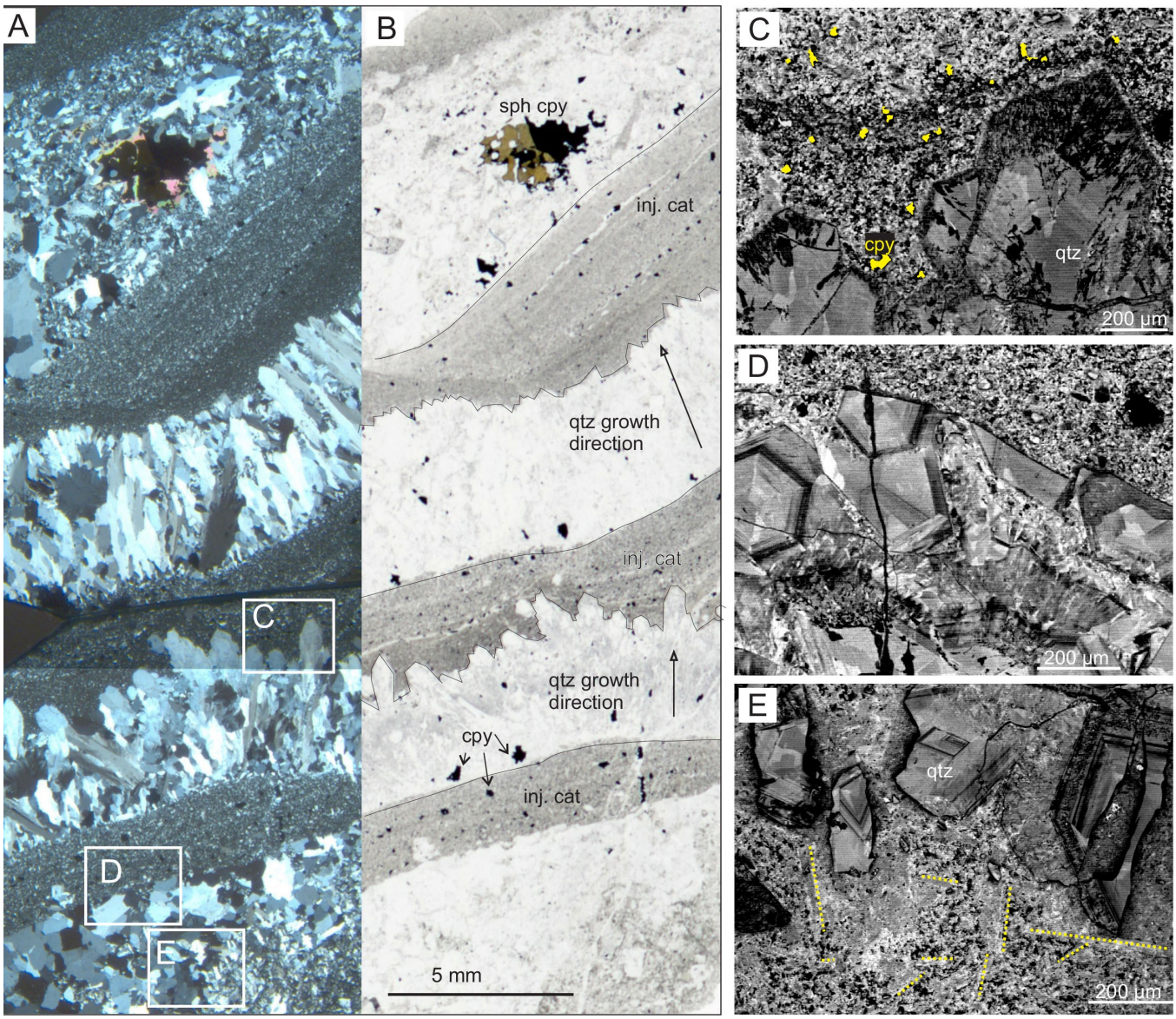

Figure 8. Photomicrographs of hydrothermal veins and episodic injected ultracataclasites. XPL (A) and PPL (B) micrographs showing episodic quartz and injected cataclasites from core zone A2. Note location of C, D and E in frames. (C) Cathodoluminescence SEM image showing zoned euhedral quartz cores with plumose-textured rims. The matrix between such quartz grains was then, later on, filled by newly injected cataclasite with chalcopyrite (yellow grains). (D) Cathodoluminescence SEM image showing fractured clasts of zoned quartz with fractures filled by injected ultracataclasite. (E) Fractured clasts of hydrothermal zoned quartz with plumose rims and surrounding infill of ultracataclasite with newly grown acicular minerals, in yellow (bottom half of photo. Abbreviations: inj. cat. – injected cataclasite, qtz – quartz, cpy – chalcopyrite, sph – sphalerite.

Domain A2 (core zone) defines a c. 4 m-thick cataclasite zone, which is texturally similar to that of domain A1, but which affected weakly foliated tonalite gneiss host rocks of the footwall. This domain has the same types and amount of cohesive cataclasites and surrounding matrix components as domain A1 (Fig. 7), and also contains an extensive network of hydrothermal veins ranging in width from 1 mm to >1 m, which makes up c. 60% of the material in this zone. This vein material is also present as matrix cement enclosing rounded to sub-angular, polymict clasts of embedded older cataclasite, tonalites, and fractured hydrothermal quartz and sphalerite grains (Fig. 11C, D). In addition, this core zone contains abundant

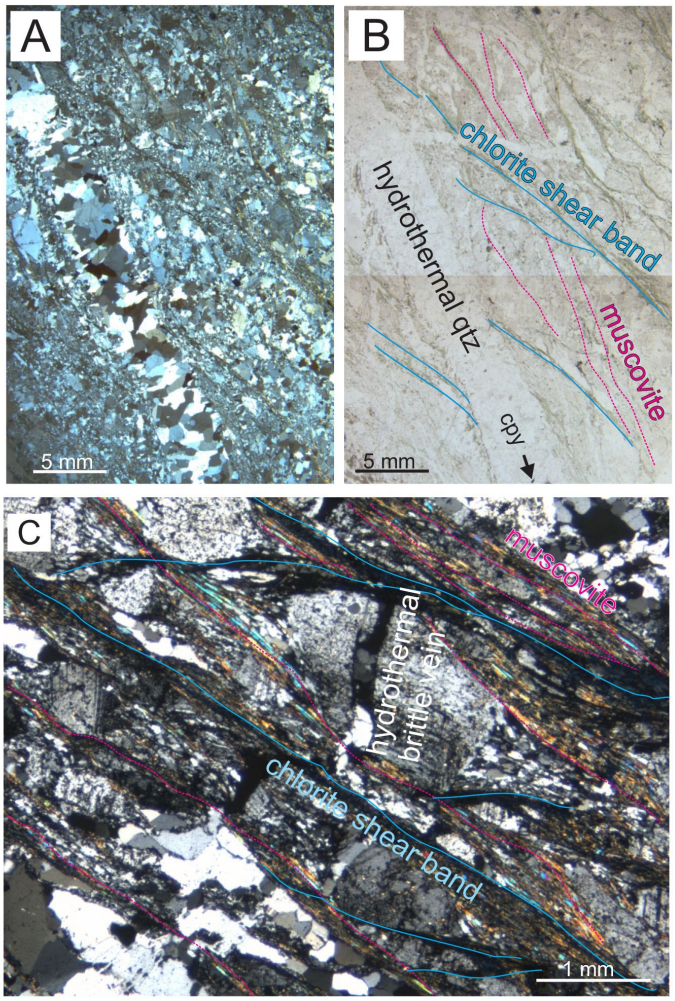

Figure 9. (A & B) XPL and PPL photomicrographs from damage zone B1 showing weakly foliated tonalite gneiss with muscovite (pink) bands cut at a low angle by chlorite shear bands (blue). Younger hydrothermal quartz and chalcopyrite veins truncate, but are arranged parallel to the old, ductile fabric of the gneisses. (C) XPL micrograph of tonalitic gneiss with foliation composed mostly of aligned muscovite, which is superposed at a low angle by chlorite shear bands in tonalite gneiss. Note the large, sigmoidal feldspar crystal in the middle of the micrograph which is fractured and dilated by quartz.

networks of pale-green ultracataclasites with internal banding (Figs. 8A–D & 11C–D). Thin-section observations show that the apparent banding of the ultracataclasites is caused by minor variations in grain size (Figs. 8A, B), and that these ultracataclasites fill open spaces between quartz veins (Fig. 8C), and/or define consolidated sub-angular clasts within quartz breccias (Figs. 8D, E & 11C). Acicular grains observed within the ultracataclasites (Fig. 8E) suggest grain growth and that the original grain size was smaller.

Domain B1 (damage zone) is c. 40 m thick and located in tonalitic gneisses of the footwall to the VBF. It defines a link zone or fracture corridor between core zones A1 and A2 (Fig. 5), and is characterised by a heavily fractured, weakly foliated tonalite gneiss with narrow (<60 cm thick) localised cataclastic zones parallel to the main and subsidiary fault surfacof the VBF. Most of the fractures are infilled with multiple cross-cutting stockwork veins (Fig. 11E), ranging in thickness from 1 mm to c. 80 cm.

In thin section, the relict gneiss foliation in the tonalitic gneiss host rock is observed as 1–2 mm-long composite bands of muscovite (Fig. 9C). This fabric is cut at a low angle by semi-brittle, chlorite-rich shear bands (Figs. 9A–C), indicating that the fracturing produced a retrogressed shear-band texture. Larger (<2 mm) plagioclase grains have commonly healed microfractures filled by microcrystalline quartz and chlorite; some are dilated by hydrothermal veinlets (Fig. 9C).

Domain B2 (damage zone) is c. 15 m thick and present in the footwall of core zone A1 (Fig. 5). This fractured zone is located mainly within a thick, foliated, metagabbro dyke, and it is truncated by networks of irregular brittle fractures, locally with narrow <40 cm thick) cataclasite zones. Most of the fractures are

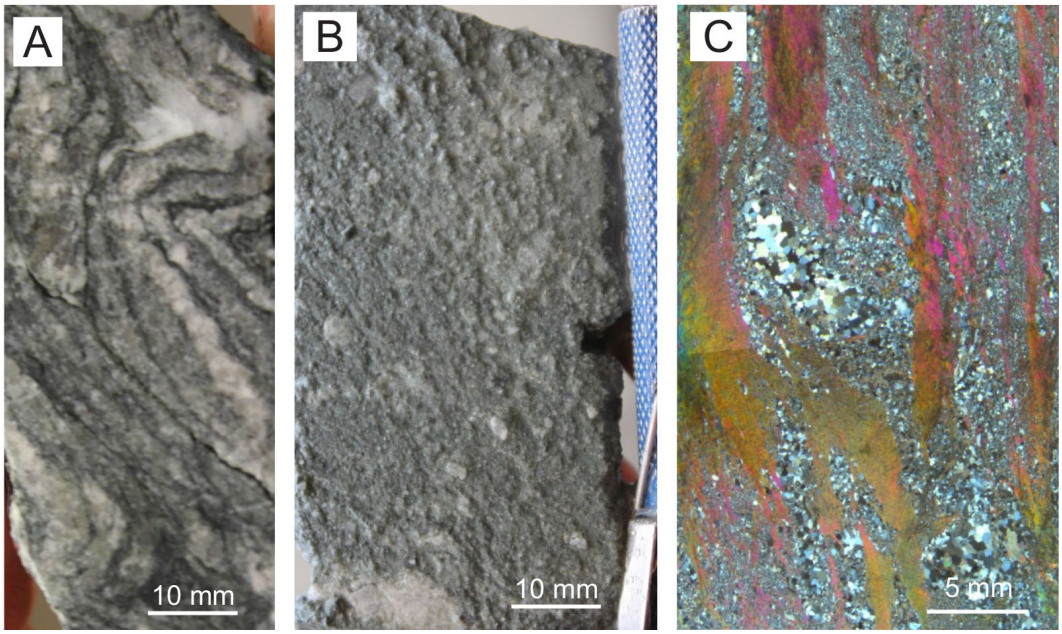

Figure 10. (A) Hand-specimen photo of folded, well-foliated, non-mineralised quartz-mica schist in Skipsfjord Nappe host rocks of the hanging wall to the VBF. (B) Hand-specimen photo of unconsolidated fault gouge (core zone A2) at the contact between quartz schists in the hanging wall and the mineralised footwall of the VBF. (C) Photomicrograph (XPL) of quartz-mica schists from Skipsfjord Nappe rocks showing the muscovite foliation and a sigmoidal-shaped quartz crystal.

filled by chalcopyrite-bearing quartz and calcite veins (Fig. 11F, G). In contrast to the damage zone of domain B1, the quartz veins define parallel sets of sheeted veins close to the core zone, changing texturally into stockwork vein networks with a more random orientation when farther from the core zone.

The typical mode of the foliated metagabbro identified in thin-section is 70% dark-green, strongly pleochroic amphibole, 20% partly sericitised plagioclase, 10% fine-grained quartz as well as trace amounts of magnetite, garnet and ilmenite. In the fractured metagabbro, amphibole and ilmenite/magnetite grains are partly to completely replaced by chlorite, quartz, anorthite feldspar, and minor pyrite, titanite, apatite and rutile. Hydrothermal alteration of the metagabbroic host rock is outlined texturally as haloes along contacts to quartz veins and stock networks (Fig. 11F).

Domain C (hanging wall) represents the down-dropped hanging wall strata of the Skipsfjord Nappe (Fig. 5) with strongly foliated quartz-mica schists and intercalated mafic schists and lenses (Fig. 10A). In contrast to the core and damage zones of the VBF, the hanging wall schists are less fractured and lack Cu or Zn-bearing hydrothermal mineralisation (Fig. 5). The contact with cataclasites of the VBF itself (Fig. 5, domain A2) is marked by a narrow c. 1–2 m-thick zone of unconsolidated, green-coloured fault gouge with sub-rounded clasts of quartz (≤1 cm) in a fine-grained, clay-rich matrix (Fig. 10B) composed of illite and smectite–vermiculite (cf., Davids et al., 2013). This gouge zone is irregular in shape and may disappear along strike, but where present it truncates (post-dates) the cataclasites of domain A2. No hydrothermal veining or mineralisation is observed in the gouge material.

In thin-section, alternating layers of recrystallised quartz (50%), white mica (40%), and plagioclase (10%) make up the ductile foliation of the Skipsfjord Nappe schists with accessory tourmaline (dravite), apatite and uranothorite. The foliation itself shows clear evidence of internal shearing, by sigmoidal quartz porphyroblasts, mica fish and remnants of intrafolial tight folds (Fig. 10C). These ductile fabrics are all truncated by the brittle VBF.

Domain D (footwall) represents weakly foliated basement tonalite gneiss in the footwall to the VBF. This domain is weekly fractured and contains no significant mineralisation.

Hydrothermal veins hosting Cu–Zn mineralisation

Hydrothermal networks of Cu–Zn-mineralised quartz and calcite veins exist in variable amounts and geometric relationships both in the core (domains A1–A2) and in the damage zones (domains B1–B2) of the VBF (Fig. 11). In the core zones, matrix-bearing cataclasites are the main mineralised zones, whereas in the damage zones, secondary quartz and calcite are present as mineralised stockwork and/or parallel/sheeted veins. Notably, complex and multiphase microtextural and cross-cutting relationships of the Cu–Zn-bearing veins are observed (Fig. 11H–L). These relationships provide the basis for evaluating temporal and mineralogical changes of the hydrothermal veins/fluids. By use of such criteria, we propose a succession of veining from early to late-stage as: (i) quartz-sphalerite (QS) veins (10–30 mm wide; Fig. 11A), (ii) quartz-chalcopyrite (QCp) veins ± calcite (1 mm to 1 m wide; Figs. 11C, D, F, G), (iii) calcite (Ca) veins (5 mm–1 m wide; Fig. 11B), and (iv) minor narrow (<10 mm wide) quartz-calcite-fluorite-sulphosalt veins (QCF) (Fig. 11H, I). Further details of these vein types are as follows:

QS veins (stage i) are mainly restricted to core zone A1 (Fig. 5) and are characterised by euhedral, zoned and massive quartz associated with sphalerite mineralisation (Fig. 11A, H, I). Sphalerite is brown to deep orange in colour (Fig. 11A, B, H), commonly colour zoned, and is observed both as small (<1 mm) inclusions within larger (<10 mm) quartz grains and as interstitial material between quartz grains (Fig. 11I). In addition to vein style mineralisation (Fig. 11H), individual grains of quartz and sphalerite are partly dismantled and now present as clasts within even younger generations of cataclasites (Fig. 11A, B, J–L), and truncated by a younger generation of quartz-chalcopyrite veins (QCp veins; Fig. 11J–L). These textural relationships indicate that the QS veins are the earliest observed hydrothermal veins.

QCp veins (stage ii) are composed of quartz and chalcopyrite with minor calcite. They constitute the most voluminous and spatially most extensive generation of quartz veins, and in contrast to QS veins are present in both the core and the damage zones. Within the core zones (Domains A1, A2), quartz of the QCp veins exists as fine-grained matrix and as massive to euhedral grains in a hydrothermal breccia, enclosing rounded to sub-angular, displaced polymict clasts of basement tonalite gneiss, injected cataclasite (Fig. 11C), and earlier generations pf hydrothermal quartz and sphalerite (QS veins; Fig. 11A). Within the damage zones (Domains B1, B2), these quartz-chalcopyrite veins define cross-cutting stockwork -veins or parallel sets of sheeted veins (Fig. 11E–G). In both cases, chalcopyrite is commonly deposited as a rim around clasts or at the inner edges of the veins (Fig. 11C), in direct contact with Fe-bearing minerals like chlorite or pyrite, or in contact with chlorite-rich cataclasite (Figs. 8C & 11D).

Notably, within the core zone of domain A2, multiple repeated quartz veins and injected ultracataclasites are observed (Fig. 8A, B), outlined by euhedral quartz grains growing from the vein wall and having zoned cores and feathery/plumose textures on the rims (Fig. 8C–E). In addition, injected cataclasite is also present as fracture infill (Fig. 8D) and as matrix within broken hydrothermal quartz clasts (Fig. 8E). Multiple criss-cross networks of QCp veins exist, but an attempt to separate them into further generations and/or sub-stages has not been successful.

Ca veins (stage iii) are characterised by various barren carbonate (calcite) veins cross-cutting veins of previous generations, or in conjunction with minor sphalerite and chalcopyrite. Calcite, however, is also present in all other vein types, where it represents the last infill stage in veins, and such calcite clearly post-dates the deposition of sphalerite (Fig. 11J–L), since sphalerite grains are fractured and show a jigsaw pattern. Calcite matrix observed in a coarse-grained breccia at the top of core zone A1 (Fig. 11B) with

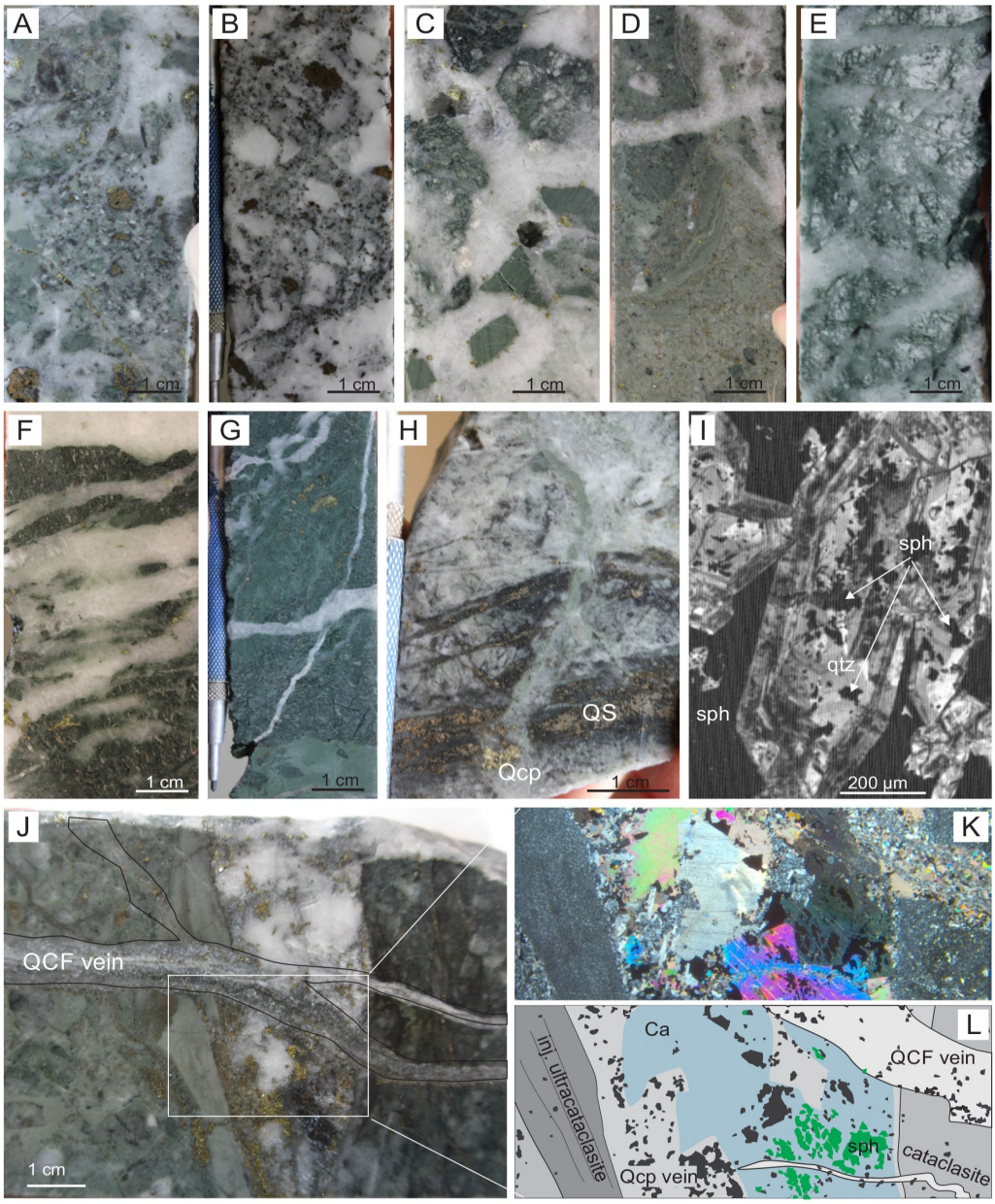

Figure 11. Drillcore photographs (A–H, J) and photomicrographs (I, K & L) of typical mineralisation textures and quartz-carbonate veins. (A) Cataclasite with enclosed, early-stage sphalerite mineralisation (QS) outlined as clasts cemented by a later phase of quartz-chalcopyrite veining material (QCp). From core zone A1. (B) Calcite-cemented sphalerite-rich breccia located at the top of core zone A1 (see Fig 5). (C) Clasts of banded ultracataclasites cemented by hydrothermal (QCp) veins in cataclasite of domain A2. Note that chalcopyrite is present as rims around chlorite-bearing clasts. (D) Cataclasite from core zone in domain A2, with clasts of quartz and several older generations of cataclasite, cemented by injected ultracataclasites, and cross-cut by hydrothermal quartz veins. (E) Damage zone B1 is characterised by fractured and weakly foliated tonalite gneiss cut by stockwork QCp veins and chlorite alteration. (F) Chloritised gabbro in damage zone, domain B2, cut by parallel QCp veins. (G) Fine-grained cataclasite cut by QS veins in damage zone, domain B2. (H) Direct cross-cutting relationship between early QS veins and later QCp veins, in core zone A1. (I) SEM cathodoluminescence image of a QS vein. Note the zoned, euhedral quartz crystals with sphalerite occurring as small inclusions in quartz, and as interstitial phalerite between quartz crystals. (J) Cross-cutting relationships observed in core zone A1: Injected ultracataclasite is cut by QS and QCp veins, with a later infill of massive calcite. Early sphalerite grains are fractured in a jig-saw pattern by the later calcite infill. A narrow QCF vein with massive textures is the youngest vein observed. (K, L) Uninterpreted XPL (K) and interpreted (L) photomicrograph of a portion (frame) of sample (J) outlining the relative timing (stages i–iv) of QS (green sphalerite), QCp (pale-grey quartz and black chalcopyrite), Ca (pale-blue calcite and black chalcopyrite), and QCF veins (palest white quartz-calcite-fluorite and black chalcopyrite and Pb-Ag-Bi sulphides), respectively. Injected cataclasites with apparent banding are outlined in the darkest grey colour.

a large number of sphalerite clasts is also interpreted to be a late-phase Ca vein. However, the lack of cross-cutting relationships with QCp veins makes this interpretation uncertain.

QCF veins (stage iv) are the youngest veins observed in the VBF, and they are only identified locally in core zone A1. These are narrow veins (<4 mm) of equant grains of massive quartz, calcite, fluorite and notably with Pb–As–Ag–Bi sulphides (Fig. 11J–L). This vein type will not be discussed further because of its limited spatial extent.

Alteration mineralogy and chlorite geochemistry

The secondary minerals associated with each of the above-described vein types are commonly expressed as alteration haloes along rims of quartz veins, but the mineral assemblages change as these veins extend into the different host-rock types. Chlorite is the dominant alteration mineral and gives the altered rocks a pale-green colour. In cataclasites, chlorite is found in close association with the main gangue minerals such as quartz and calcite, but also with minor albite, clinozoizite, titanite, rutile, apatite and cookeite. In tonalitic host-rock gneisses of the footwall to the VBF, chlorite (±titanite) replaces host-rock biotite and amphibole. Some epidote alteration of feldspar is also observed. In the gabbroic dyke host rock, tabular amphibole is replaced by chlorite and titanite/rutile; most feldspar is partly or fully replaced by epidote/ clinozoizite; and ilmenite/magnetite is partly replaced by pyrite/chalcopyrite and titanite (Fig. 12). XRD analyses of very fine-grained ultracataclasite rocks show that quartz, chlorite, chalcopyrite and minor aggregates of microcline have completely replaced the original mineralogy.

We analysed the mineral chemistry of fine-grained chlorite present as matrix in cataclasites in core zones A1 and A2 of the VBF (Fig. 13), with an aim to estimate the temperature of the hydrothermal alteration (Table 1). Chlorites were selected for analysis based on textural proximity to Cu–Zn-bearing veins, to ensure that they were formed synchronously.

The chemical composition classifies the chlorite as clinochlore to chamosite (Table 1), with formation temperatures ranging from 280 to 305°C ± 30°C (Cathelineau, 1988). For example, chlorite analysed from surface outcrops of cataclasite in core zone A2 indicated a temperature of 280°C (Fig. 13A), whereas analysed chlorite from core zone A1 in drillcores at 70 m depth yielded a temperature of c. 295°C. In addition, at 93 m depth in domain B2, two generations of chlorite in the gabbroic host rocks (Fig. 13B) displayed a drop in the Mg/Fe ratio from core to rim, where the Mg-rich chlorite in the core indicates a formation temperature of 285°C, while the Fe-rich rim indicates growth at 305°C (cf., Table 1).

Fluid inclusion

The fluid inclusion study was conducted on quartz, calcite and sphalerite from three generations of hydrothermal veins (i.e, QS veins, Fig. 14A; QCp veins, Fig. 14B; and Ca-veins, Fig. 14C). The microthermometric measurements were used to determine the salinity and density of the hydrothermal fluids that circulated along the VBF, as well as to indicate P-T-X conditions during faulting events. Further, the resulting fluid properties were used to infer the metal solubility potential of the ore-forming fluids and investigate the depositional mechanisms.

Fluid inclusion petrography

Primary fluid inclusions occur along growth zones and within isolated clusters. Primary fluid inclusion assemblages are usually cross-cut by trails of less common pseudosecondary and secondary inclusions (Fig. 14K). The microthermometry was conducted only for primary and pseudosecondary fluid inclusions, whereas the small size of secondary inclusions (<2 µm) precluded reliable measurements. Based on their

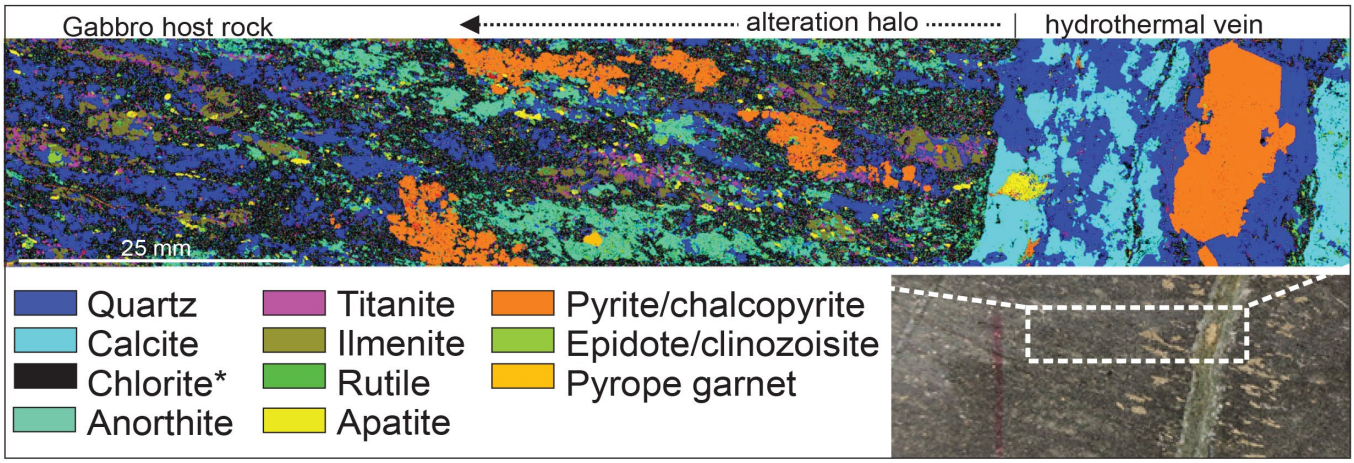

Figure 12. Secondary mineral growth expressed as an alteration halo adjacent to a QCp vein, in gabbro from damage zone B2 (see inset photo of hand-specimen and location of section, white stippled frame). SEM EBSD image (upper part) showing secondary alteration minerals replacing original minerals (in colour) along existing foliation in gabbro. The QCp vein is composed of quartz, calcite and pyrite/chalcopyrite, with minor apatite and epidote. The mineral replacement is more pronounced close to the QCp vein where amphibole is replaced by chlorite; ilmenite/magnetite is replaced by pyrite/chalcopyrite and titanite; and feldspar is partly replaced by epidote.

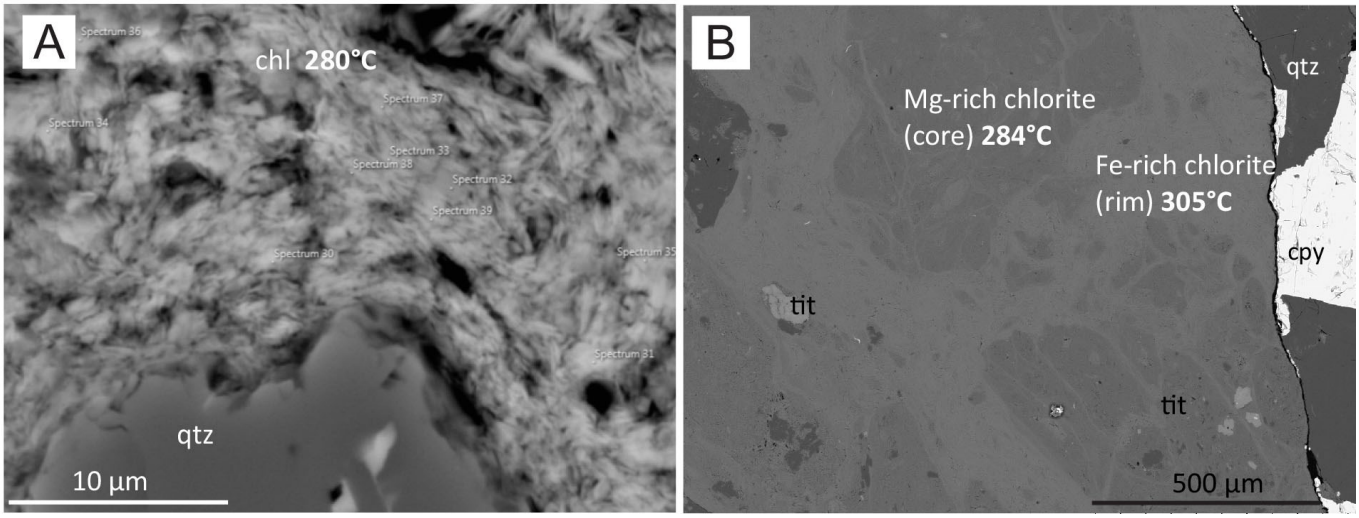

Figure 13. SEM images of different chlorite associations analysed for chlorite geothermometry. (A) Fine-grained chlorite in cataclasite from the top of core zone A1. (B) Two generations of cataclasite with chlorite alteration of amphibole in gabbro dyke in damage zone B2.

Table 1. Chemical compositions of secondary chlorite formed in haloes of injected QCp hydrothermal veins in core-zone cataclasites of the VBF, associated with mineralisation. The formula is calculated on the basis of 14 oxygens. Mdn ± σ – median value plus/minus one standard deviation.

Sample-depth (m)	n	Material analysed	Domain	Chlorite type	SiO_2 (%) ± σ	Al_2O_3 (%) ± σ	FeO (%) ± σ	MnO (%) ± σ	MgO (%) ± σ	Total ± σ	Temp (°C)*	Average structural formula
V6 -surface	8	Cataclasite	A2	Clinochlore	27.4 ± 0.9	19.4 ± 0.7	22.9 ± 1.1	0.6 ± 0.1	14.5 ± 0.7	84.7 ± 2.1	280°C	$(Mg_{2.33}Fe_{2.06}Al_{1.40}Mn_{0.05})(Si_{2.94}Al_{1.06})O_{10}(OH)_8$
101-70.5	8	Cataclasite	A1	Chamosite	28.9 ± 0.7	19.4 ± 0.6	28.3 ± 1.2	0.7 ± 0.1	15.7 ± 0.8	93.0 ± 1.0	295°C	$(Mg_{2.35}Fe_{2.37}Al_{1.18}Mn_{0.03})(Si_{2.89}Al_{1.11})O_{10}(OH)_8$
101-93	10	Mg-rich core cataclasite	A1	Clinochlore	27.5 ± 0.6	18.5 ± 0.6	19.4 ± 1.2	0.1 ± 0.1	18.3 ± 0.9	84.0 ± 1.4	285°C	$(Mg_{2.61}Fe_{2.00}Al_{1.26}Mn_{0.01})(Si_{2.93}Al_{1.07})O_{10}(OH)_8$
101-93	8	Fe-rich rim cataclasite	A1	Chamosite/ Clinochlore	25.7 ± 0.4	18.6 ± 0.3	24.9 ± 0.4	0.4 ± 0.2	13.8 ± 0.6	83.4 ± 1.1	305°C	$(Mg_{2.28}Fe_{2.31}Al_{1.30}Mn_{0.03})(Si_{2.86}Al_{1.14})O_{10}(OH)_8$

** formation temperature calculated using the geothermometer of Cathelineau (1988).*

petrographic characteristics, primary and pseudosecondary inclusions from all three generations of veins can be divided into three types:

Type 1 represents primary multiphase (liquid-vapour-solid) inclusions (Fig. 14D) containing an aqueous liquid (70 vol.%), a vapour bubble (15 vol.%), and a cubic solid phase (halite) (15 vol.%). In places, assumed incidentally entrapped phases of elongated/tabular or fibroradial minerals are also observed (Fig. 14E). Type 1 inclusions are generally sub-rounded or with negative crystal shapes. These inclusions are found in all vein types, but mostly in QS veins, in both quartz (Fig. 14D) and sphalerite (Fig. 14F). In QCp veins they are much less frequent and are hosted within the cores of euhedral and zoned quartz. Type 1 inclusions are also found in Ca veins.

Type 2 inclusions are also primary in their origin but, in contrast to Type 1, they do not contain a cubic solid phase. According to their petrographic properties, inclusions of this type can be divided into two subtypes, Type 2a and 2b. Type 2a inclusions are two-phase inclusions (liquid-vapour) that have sub-rounded to negative crystal shapes and contain a liquid phase (80 vol.%) and a vapour phase (20 vol.%; Fig. 11G, H). Type 2a inclusions are found in sphalerite and in calcite. Type 2b inclusions are irregularly shaped and, in addition to liquid (75–80 vol.%) and vapour (15–20 vol.%), can also contain between <1 to 10 vol.% of solid phase(s) that are irregular, tabular or radiating tabular in shape (Fig. 14I, J). Type 2b inclusions are found in quartz from both QS and QCp veins.

Type 3 inclusions are pseudosecondary inclusions grouped in narrow trails of coexisting, small (<20 µm), L + V and monophase L-only inclusions (Fig. 14K). The L + V inclusions have c. 90–98 vol.% liquid and 2–10 vol.% vapour, while L-only inclusions (at room temperature) commonly developed a vapour bubble during the freezing cycle. Type 3 veins are found in QS vein quartz.

Fluid inclusion microthermometry

Microthermometric measurements were performed on fluid inclusions in quartz, calcite and sphalerite. However the most numerous data, were obtained from fluid inclusions in quartz, because they are generally larger and easier to measure accurately. By contrast, fluid inclusions in sphalerite were usually too dark for phase changes to be observed, whereas calcite-hosted inclusions are too small (<20 µm).

During the freezing cycle, all fluid inclusions were undercooled to -100 to -130°C. Upon heating, frozen inclusions would turn dark brown at around -80°C followed by first melt occurring at the T_e of around -52°C indicating a fluid composed of H_2O–NaCl–$CaCl_2$ (cf., Roedder, 1984; Steele-MacInnis et al., 2011). Fluid inclusions in the H_2O–NaCl–$CaCl_2$ system are notorious for metastable behaviour, which includes absence of phases that are expected to be present and occurrence of phases that are not expected to be present (Chu et al., 2016). In the following, we will describe the behaviour of each type of fluid inclusion and also note assumptions, possible metastable behaviour, and present alternative calculations for salinities. Despite uncertainties in the salinity calculations, the accuracies of the salinities presented is acceptable within the scope of this paper.

Type 1 (L + V + H) inclusions froze to a dark fine-grained mass during the freezing cycle. When heated the inclusions would turn dark brown at around -80°C followed by first melt occurring around a T_e of around -52°C. Ice, observed as a globular transparent phase, melted over a large range of temperatures from -52.3 to -37.5°C. It is assumed that this is antarcticite that melts at the eutectic temperature. Upon further heating, the isotropic solid in Type 1 inclusions melted at around +70 to +151°C, and total homogenisation was characterised by a vapour to liquid transition in the temperature range from +70 to +239°C. The elongated solid was insoluble up to 400°C. Based on the eutectic temperature of -52°C, total salinities are expressed as NaCl + $CaCl_2$ wt.% according to Steele-MacInnis et al. (2011). The total salinity for Type 1 inclusions was calculated from the peritectic $T_{m\ Ice}$ and final melting temperature of halite (T_s) based on the methods of Vanko et al. (1988). This resulted in salinities of 33–36 wt.% NaCl + $CaCl_2$ (Table 1). However, it should be noted that in some Type 1 inclusions, poor optical properties hindered accurate measurement of $T_{m\ Ice}$ and for these inclusions salinities are calculated based on ice (and antarcticite) melting at the eutectic;

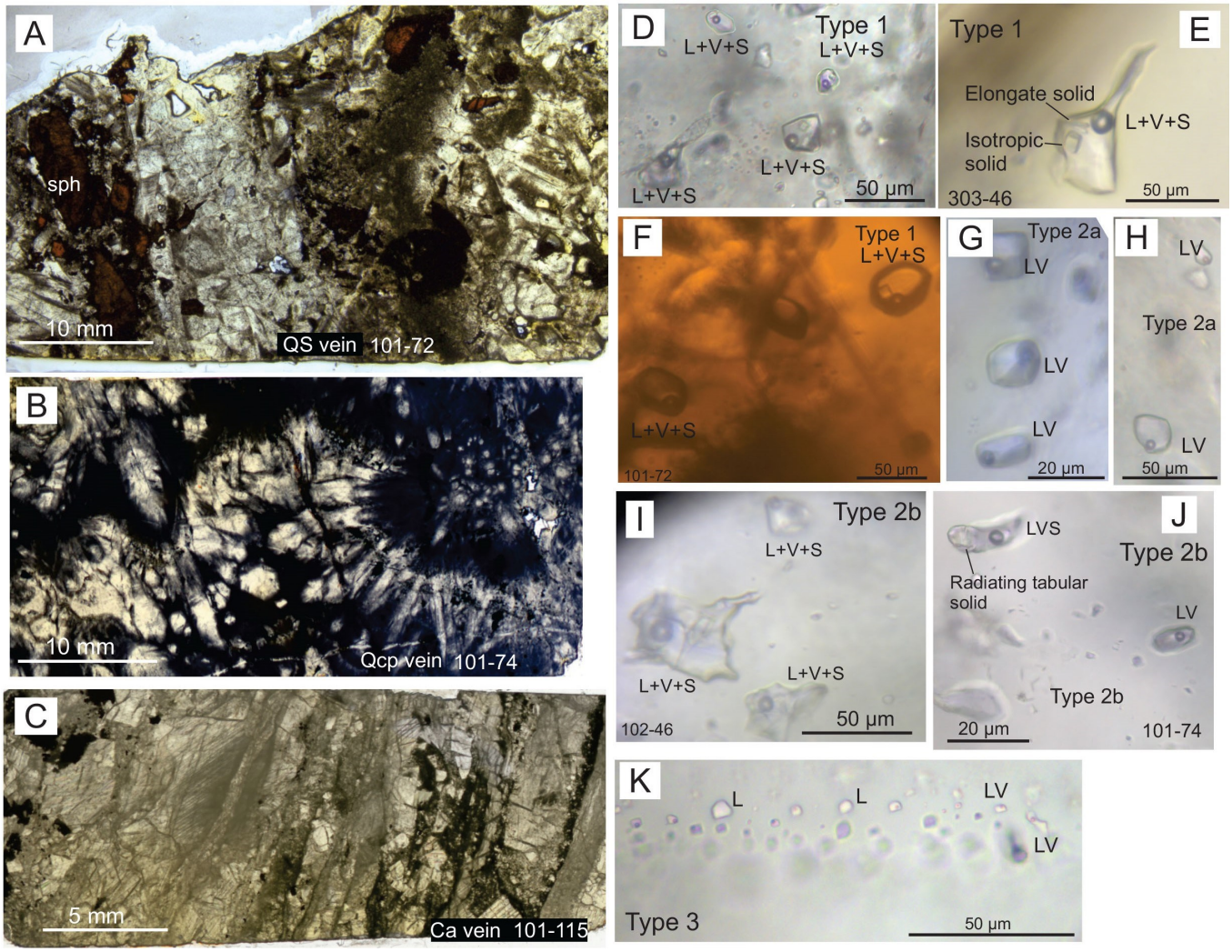

Figure 14. Compiled photographs double-polished wafers (A–C) and photomicrographs of selected fluid inclusion types (D–K). (A) Double-polished wafer of QS vein from core zone A1. (B) Double-polished wafer of typical textured QCp vein where quartz has zoned cores and feathery/plumose rims. (C) Double-polished wafer of brecciated Ca vein. (D) Composite photo of type 1 L + V + S fluid inclusion in quartz with cubic solid. (E) Type 1 inclusion in quartz with two types of solids; an isotropic cubic solid which commonly melted at around 70–200°C and a second, less common, elongate tabular crystal that did not melt when heated. The latter is possibly an incidentally entrapped solid. (F) Type 1 L + V + S inclusions in sphalerite. (G & H) Type 2a L + V inclusions in calcite. (I) Type 2b L + V + S inclusions in quartz with <1–10% solids. (J) Type 2b inclusion in quartz that contain a radiating tabular solid. (K) Type 3 L + V and L-only pseudo-secondary inclusions in quartz with negative crystal shapes. Note that L-inclusions lack vapour bubbles at room temperature, but may develop vapour bubbles during freezing.

this assumption yields higher salinities (up to 5 wt.% NaCl + $CaCl_2$) and higher NaCl/$CaCl_2$ ratios (up to 0.5). Further, salinities for Type 1 inclusions can also be calculated as NaCl wt.% equivalents using halite melting temperatures according to Bodnar & Vityk (1994); such a calulation would yield salinities in the range of 27 to 30 wt.% NaCl equivalents. $T_{m\ Ice}$ temperatures observed below the eutectic and possible for the $CaCl_2$ system (<-52°C; Steele-MacInnis et al., 2011) were interpreted as metastable (Wilkinson, 2001). Salinities for these inclusions were calculated based on a $T_{m\ Ice}$ of -52°C.

Type 2 inclusions showed two styles of freezing when cooled; either 1) the inclusion froze to a dark fine-grained mass; or 2) the inclusion did not freeze and no phase transitions were observed. No correlation between the content of the fibroradiate solids and freezing style was observed. Upon warming the frozen

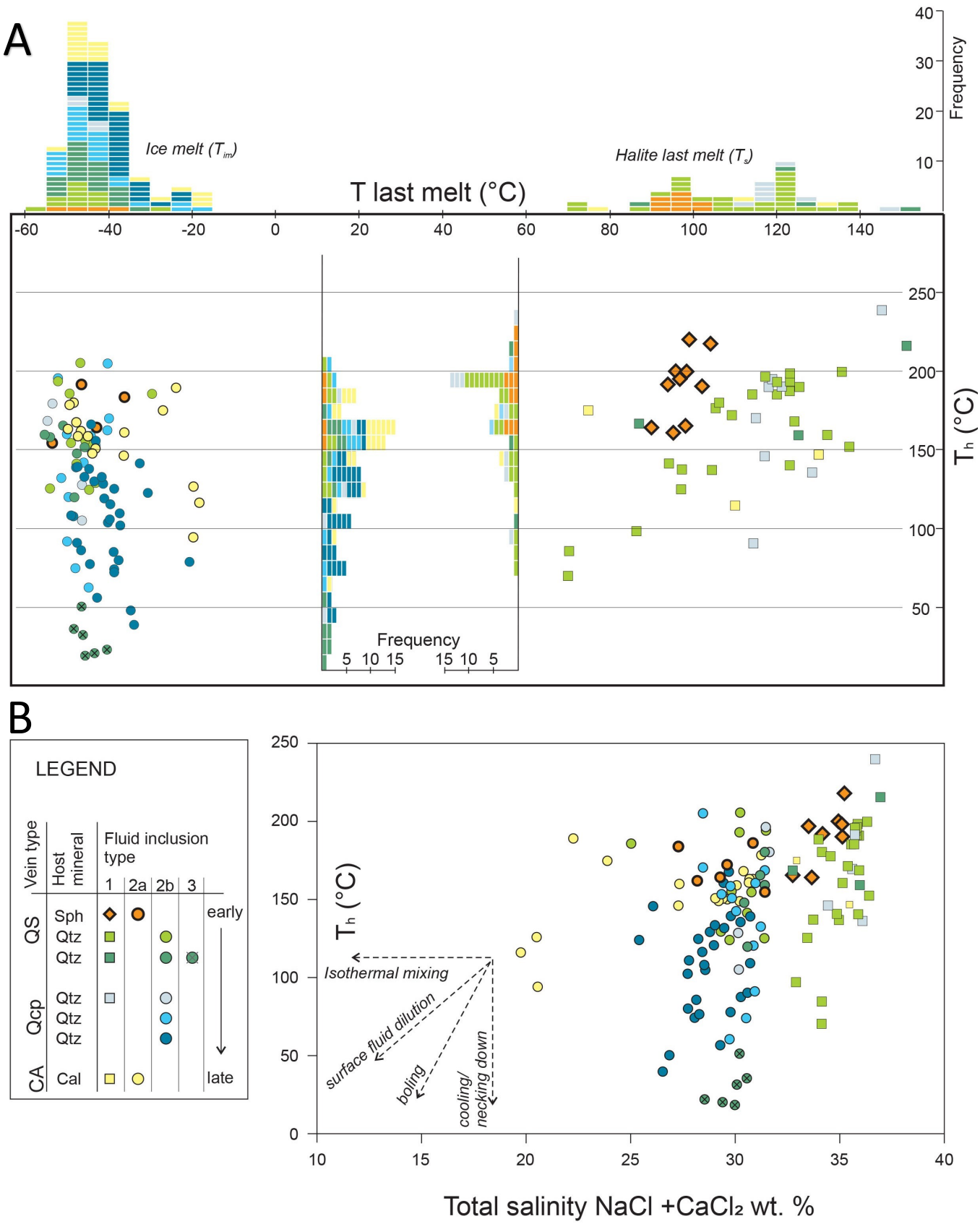

Figure 15. Summary of fluid inclusion microthermometric data. (A) Measured ice-melting temperatures ($T_{m\ Ice}$) for Type 2a, 2b and 3 inclusions are plotted on the X-axis. Halite melting temperatures for Type 1 inclusions are also plotted along the same axis. Homogenisation temperatures T_h (°C) are plotted on the Y axis. Note that frequency histograms are plotted separately for all measurements. (B) Calculated total salinity (NaCl + $CaCl_2$) vs. T_h (see also Table 2). The colours correspond to different vein samples from different vein types. Temporal relationships indicated in the legend are based on cross-cutting relationships described in the text.

Table 2. Summary of fluid inclusion microthermometry from quartz, sphalerite and calcite in hydrothermal veins. Abbreviations; P – primary inclusion, PS – secondary inclusion; SPH – sphalerite; QTZ – quartz; CA – Calcite, Mdn ± σ – median value plus/minus one standard deviation, n – number of fluid inclusion analyses.

				Microthermometric data										
Host mineral	Vein type	Incl. type	P/ PS	T_{im} (°C)		T_s (°C)		T_h (°C)		Salinity (NaCl + $CaCl_2$)***		Ratio (NaCl/$CaCl_2$)		n
				Range	Mdn ± σ	Range	Mdn ± σ	Range	Mdn ± σ	Range	Mdn ± σ	Range	Mdn ± σ	
SPH	QS	1	P	-46.9 to -38.1	-43. ± 3.2	90 – 98	95 ± 3	164 to 197	179 ± 15.0	32.8 to 34.2	33.5 ± 0.5	0.27 to 0.34	0.29 ± 0.03	4
SPH	QS	1	P	-52*	-	96 - 104	100 ± 3	190 to 218	200 ± 10.2	34.9 to 35.2	35.1 ± 0.1	0.25 to 0.26	0.26 ± 0.01	4
SPH	QS	2a	P	-53.6 to -36.2	-42.8 ± 5.6	-	-	155 to 186	164 ± 11.0	27.3 to 31.4	29.3 ± 1.4	0.06*	-	7
QTZ	QS	1	P	-52.3 to -39.9	-44.2 ± 4.1	86 - 135	106 ± 15	97 to 199	177 ± 32.3	32.9 to 36.3	34.2 ± 1.0	0.29 to 0.36	0.31 ± 0.02	9
QTZ	QS	1	P	-52*	-	70 - 137	120 ± 19	70 to 198	171 ± 38.9	34.1 to 36.4	35.8 ± 0.7	0.21 to 0.32	0.29 ± 0.03	15
QTZ	QS	2b	P	-52.0 to -30.0	-46.7 ± 5.9	-	-	125 to 205	155 ± 29.5	25.0 to 31.4	30.2 ± 1.7	0.06*	-	10
QTZ	QS	3	PS	-48.2 to -40.3	-45.9 ± 2.6	-	-	19 to 36	22 ± 6.5	28.6 to 30.6	30.0 ± 0.7	0.06*	-	6
QTZ	QCP	1	P	-43.5 to -37.5	-41.9 ± 2.5	87 - 117	96 ± 13	146 to 167	161 ± 8.8	32.6 to 34.4	33.1 ± 0.8	0.29 to 0.34	0.33 ± 0.02	3
QTZ	QCP	1	P	-52*	-	115 - 151	121 ± 10	128 to 239	170 ± 30.3	35.6 to 36.9	35.8 ± 0.4	0.28 to 0.34	0.29 ± 0.02	15
QTZ	QCP	2b	P	-54.4 to -23.9	-44.9 ± 6.0	-	-	35 to 218	127 ± 41.6	22.5 to 31.4	29.8 ± 1.7	0.06*	-	51
QTZ	QCP	2b	P	DNF**	-	-	-	156 to 220	179 ± 20.5	-	-	-	-	15
CAL	CA	1	P	-47.5 to -43	-45.3 ± 2.3	75 - 130	103 ± 28	146 to 175	161 ± 14.4	33.0 to 35.5	24.1 ± 1.3	0.27 to 0.33	0.30 ± 0.03	2
CAL	CA	2a	P	-19.8 to -18.3	-19.7 ± 0.7	-	-	94 to 126	116 ± 13.4	19.8 to 20.6	20.5 ± 0.4	0.06*	0.06 ± 0.00	3
CAL	CA	2a	p	-50.3 to -23.5	-44.8 ± 8.3	-	-	146 to 189	161 ± 11.7	22.3 to 31.0	29.8 ± 2.6	0.06*	-	14

** assumed melted at eutectic (-52°C).*
*** DNF - Did not freeze at -130°C for 5 minutes.*
**** calculated wt.% NaCl + CaCl2 (Steele-MacInnis et al., 2011).*

inclusions would turn dark brown at around -80°C followed by first melt occurring around a T_e of around -52°C. Ice, observed as a globular transparent phase, melted over a large range of temperatures from -54.4 to -18.3°C. Total homogenisation occurred by a vapour to liquid transition in the temperature range from +35 to +220°C. The various fibroradiate solids observed in Type 2b inclusions were insoluble up to 400°C. Salinities were calculated as wt.% NaCl + $CaCl_2$ according to Steele-MacInnis et al. (2011; Table 1). It was not possible to identify which phase melted at the eutectic, antarcticite or hydrohalite; however, the differences in salinity (<0.2 wt.% NaCl + $CaCl_2$) and NaCl/ $CaCl_2$ ratios (<0.03) calculated for either option are negligible. In addition, metastable behaviour is suspected for inclusions where no freezing behaviour was observed (Chu et al., 2016). Alternatively, it is possible that freezing in these inclusions was hindered by small amounts of lithium in the fluid (Dubois et al., 2010).

Type 3 inclusions showed similar microthermometric behaviour to that of Type 2 inclusions; first melting was observed at T_e, and $T_{m\ Ice}$ occurred at -48.2 to -40.3°C, resulting in salinities of 28.6–30.6 wt.% NaCl + $CaCl_2$. The majority of Type 3 inclusions were liquid only at room temperature, but several developed vapour bubbles during freezing and T_h occurred by vapour to liquid transition at 19 to 36°C.

The microthermometric results of fluid inclusions in quartz, sphalerite and calcite from QS, QCp and Ca veins are summarised in Table 2 and Fig. 15A. Fig. 15A displays the last phase melting temperature on the X-axis; for Type 1 inclusions this is the cubic solid (halite), and for Type 2 and 3 inclusions ice melting ($T_{m\ Ice}$) is the last phase observed. Homogenisation temperatures (T_h) are plotted on the Y-axis. All together, the multiphase, two-phase and monophase fluid inclusions show that the fluids were low- to moderate-temperature (<240°C) and moderately to highly saline (13–37 wt.% $CaCl_2$ + NaCl). Fig. 15B plots total

salinity vs. T_h and show two clusters of fluid inclusions; Type 1 inclusions with higher salinities (33–36 wt.% NaCl + $CaCl_2$) and Type 2 and Type 3 inclusions with lower salinities (20–31 wt.% NaCl + $CaCl_2$). A salinity gap from c. 31 to 33 wt.% total salinity separates Type 1 from Type 2 and Type 3 inclusions in Fig. 15B. This gap could be caused by metastability by failing to nucleate NaCl near the saturation point (Roedder, 1984), or it could be a result of the assumptions used to calculate the salinities of Type 1 inclusions as outlined above.

The temporal relationships between the vein types as established by the cross-cutting relationships above are also included in the legend of Fig. 15B, and the data displayed are described accordingly. Overall, the dataset shows a general positive correlation between total salinity and T_h. This positive correlation is also observed in sphalerite-hosted inclusions in QS veins (Type 1 and Type 2a) that show a weak positive correlation between total salinities (27–35 wt.% NaCl + $CaCl_2$) ranging over a rather narrow temperature

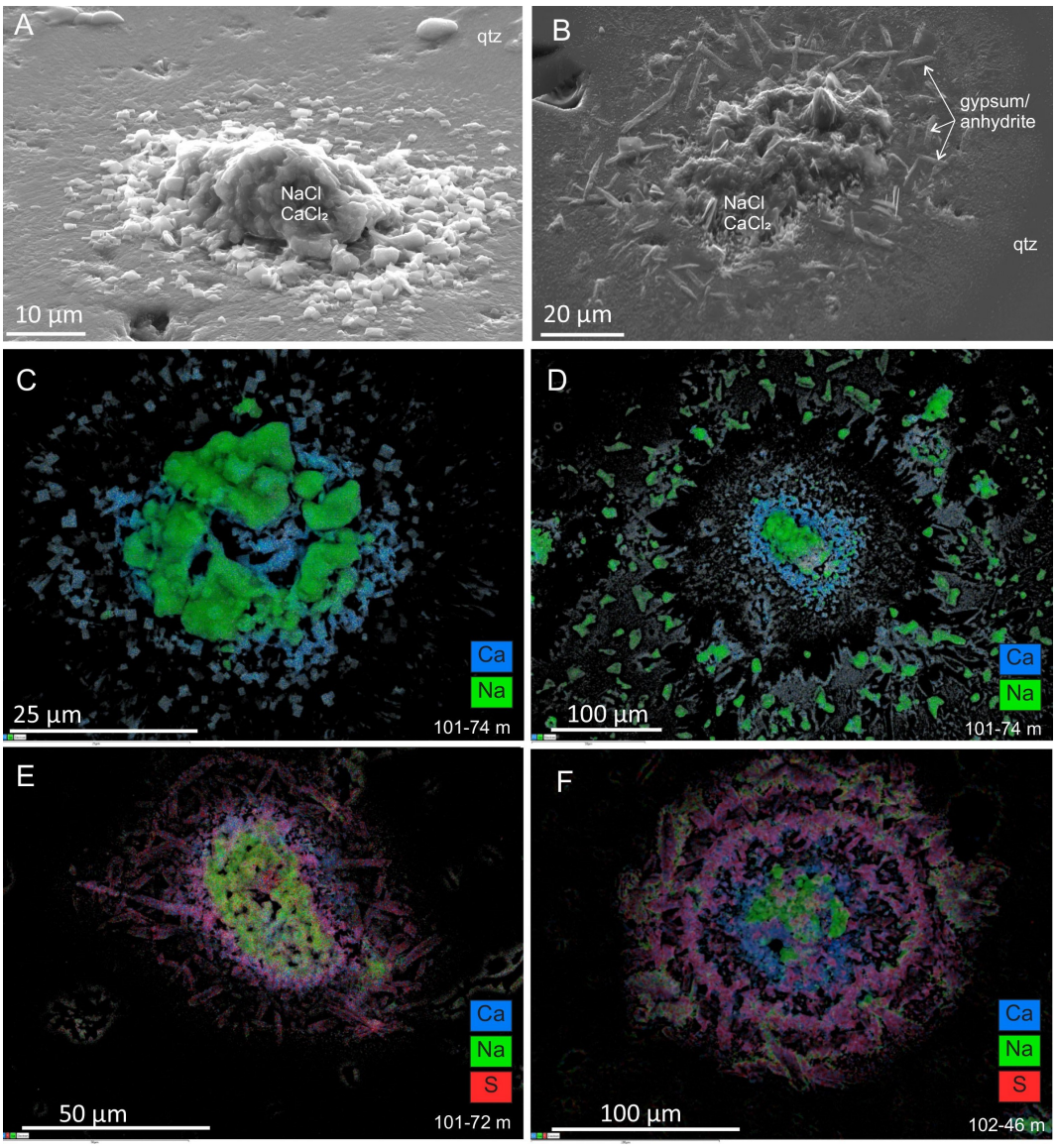

Figure 16. SEM images of evaporate mounds in quartz. (A) 3-D image of evaporate mound showing cubic NaCl and $CaCl_2$ crystals from QCP vein (sample 101-74). (B) 3-D image of NaCl, $CaCl_2$ and $CaSO_4$ crystals. (C & D) SEM-image with colour code overlay, showing distribution of Na and Ca in QCp vein (sample 101-74). (E) NaCl, $CaCl_2$ and $CaSO_4$ in evaporate mounds from a QS vein (sample 101-72). (F) NaCl, $CaCl_2$ and $CaSO_4$ in evaporate mounds from a QCp vein (sample 102-46).

range (155–218°C). Quartz-hosted inclusions (Types 1 and 2b) from QS veins are also highly saline inclusion (25–36 wt.% NaCl + $CaCl_2$) that homogenise over a larger T_h range (70–205°C). Inclusions in individual QS quartz veins (displayed as light and dark green colours) show overlap; however, the light-green vein has more inclusions with higher salinities than the vein plotted with darker green. Quartz-hosted inclusions from QCp veins show two trends, the pale-grey vein (inclusion types 1 and 2b) shows similar T_h and salinities as those from QS veins. The pale-blue and dark-blue coloured dots representing Type 2b inclusions show a relatively narrow range of salinities (25–31 wt.% NaCl + $CaCl_2$) over a large range of T_h (35–210°C). Type 3 pseudosecondary inclusions from QS veins show a weak overlap with these low-temperature Type 2b inclusions from QCp veins. Type 1 and 2a inclusions from Ca veins show the largest range in salinities (20–36 wt.% NaCl + $CaCl_2$), also with a positive correlation with T_h (94–175°C).

Fluid inclusion decrepitation

Qualitative chemical analyses of major elements in fluid inclusions in quartz were carried out by decrepitating individual inclusions and analysing the evaporate mounds formed on the sample surface (Fig. 16). SEM spot analyses of individual crystals enabled us to identify three major phases in the mounds: NaCl, $CaCl_2$, and $CaSO_4$ (anhydrite/gypsum; Fig. 16A, B). SEM map-scan analyses are presented in Fig. 16C–F and highlight the chemical composition of the mounds. Relative concentrations of Na, Ca, K, Cl and S are plotted in Fig. 17, and show two general trends based on the sulphur content: (1) mounds with varying amounts of Na, Ca, S, Cl and very minor K (e. g.); (2) mounds without S but with Na, Ca, Cl and very minor amounts of K. These trends likely reflect two different fluids.

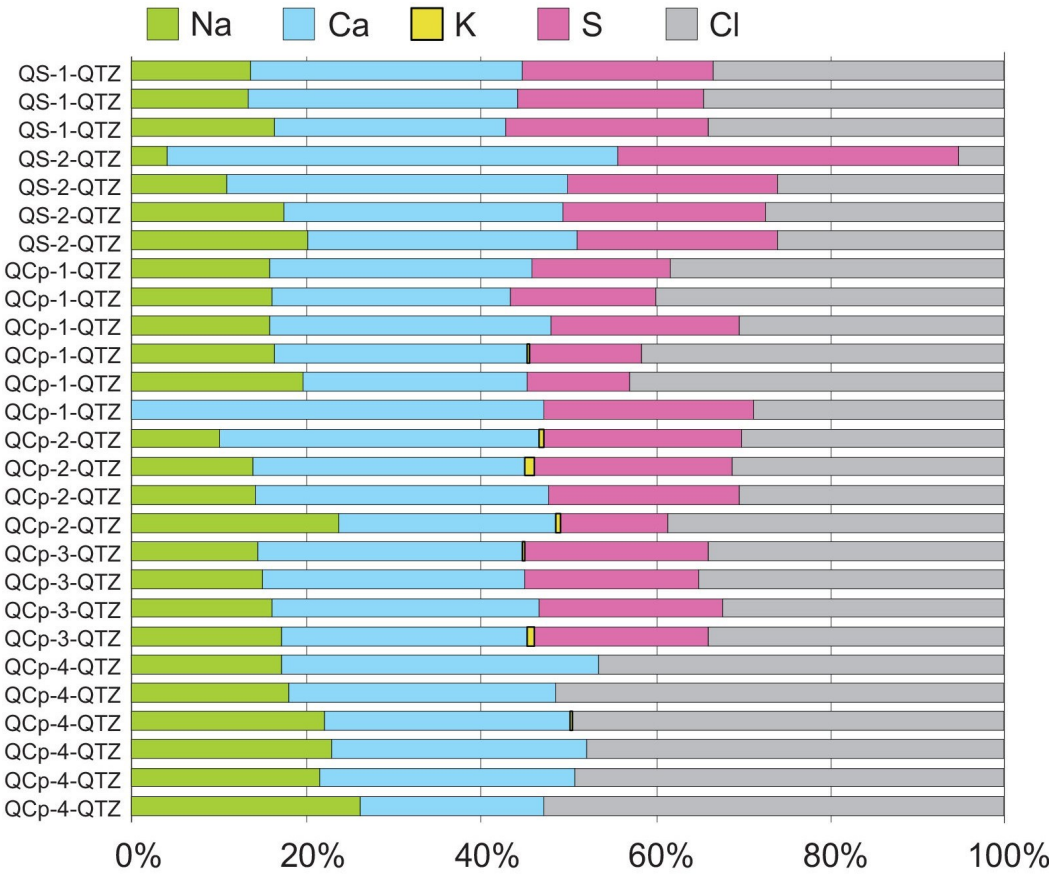

Figure 17. (A) Graphical presentation of relative proportions of Na, Ca, K, S and Cl (in wt.%) measured in evaporate mounds from decrepitated fluid inclusions in quartz. The data are obtained by surface scanning of the evaporate mounds using a SEM.

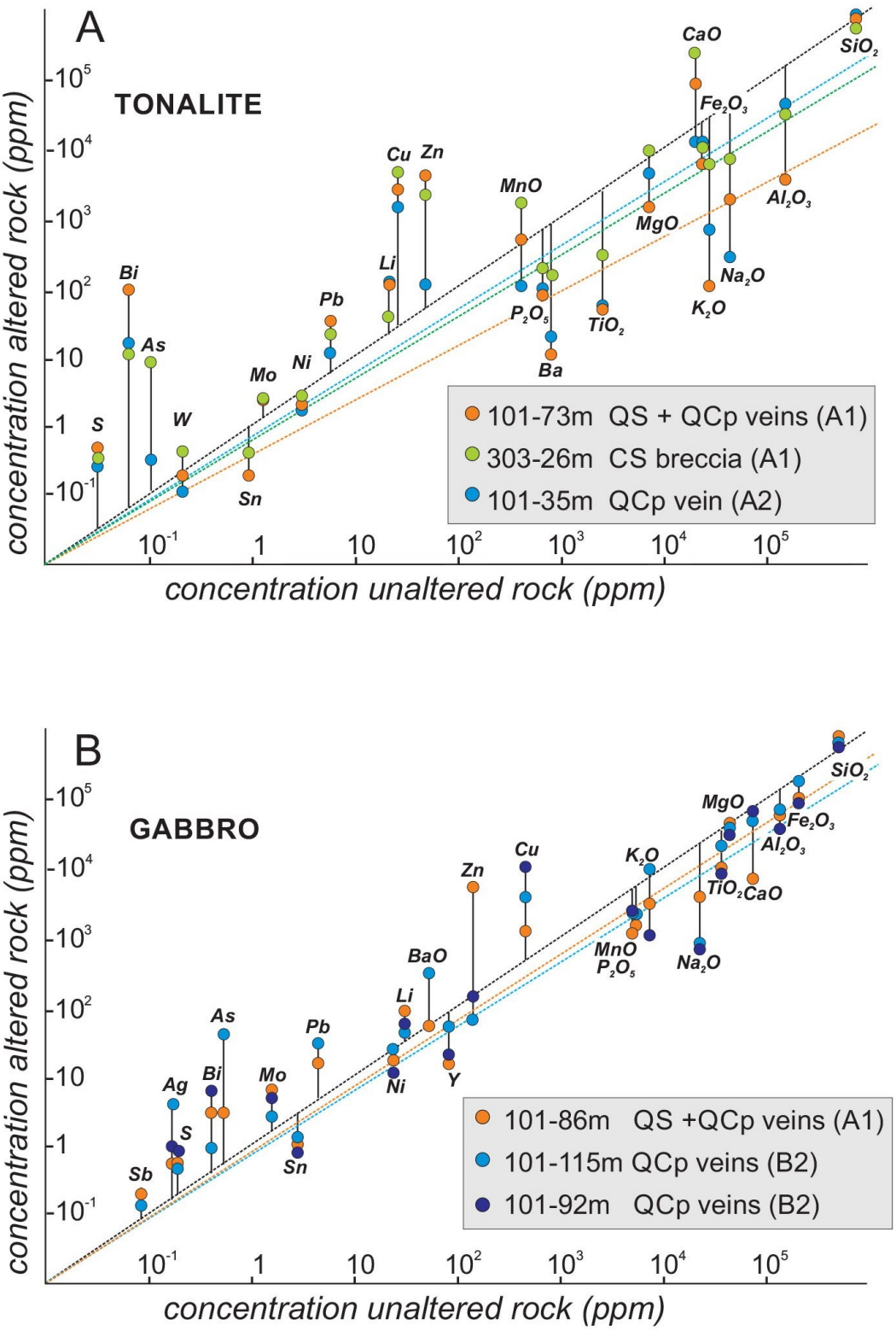

Figure 18. Isocon diagrams (after Grant, 1986) showing gains and losses of elements during fault-related hydrothermal alteration and mineralisation. Applied geochemical whole-rock data are from Store Norske Gull, drillcore sections of unaltered tonalite gneiss and gabbro, and altered host rocks, including veins and cataclasites in the core zones A1 and A2. For linear element correlations we used average line (Grant, 1986) and an additional, coloured line drawn between concentrations of presumed immobile Al_2O_3, TiO_2 and Zr. (A) Isocon diagram for altered tonalite gneiss in core and damage zones, domains A1, A2, and B1. (B) Isocon diagram for altered gabbro dyke in domains A1 and B2. Note similar alteration trends for elements in both rock types (see main text for further details).

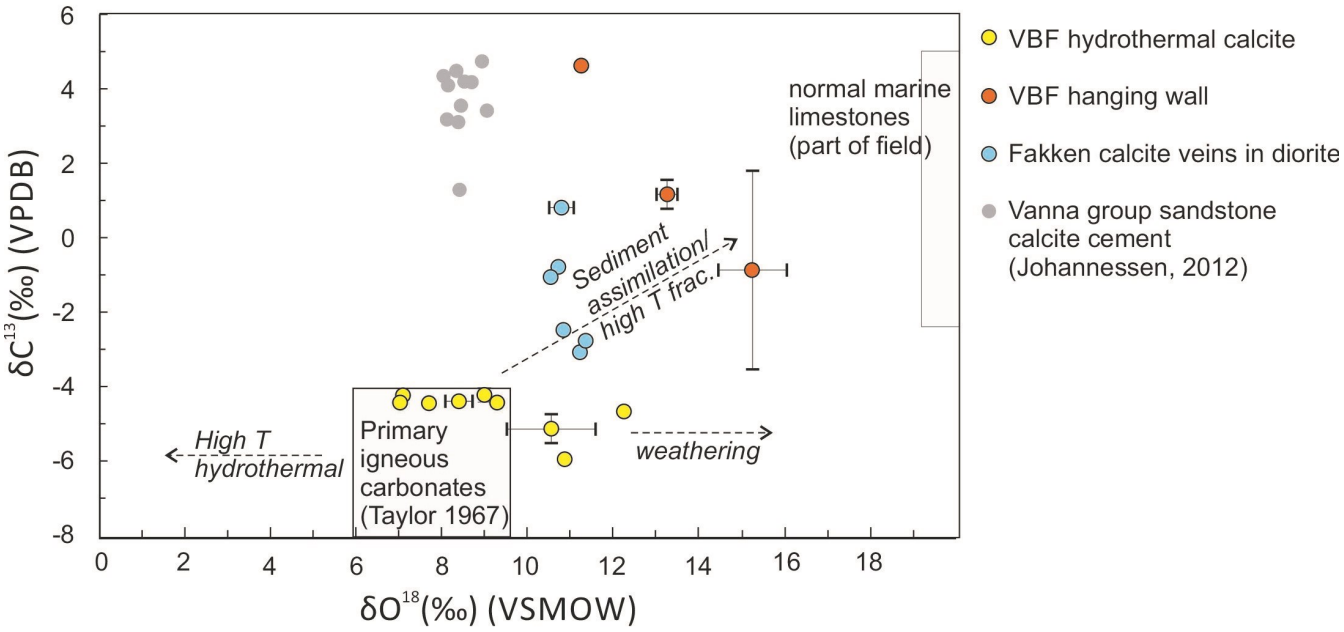

Figure 19. $\delta^{13}C$ and $\delta^{18}O$ diagram showing stable isotope composition of hydrothermal calcite from the VBF, Skipsfjord Nappe rocks in the hanging wall to the VBF, veins in diorite intruding the Vanna Group, and calcite cement from metasandstones of the Vanna Group. Note that hydrothermal calcite from the VBF overlaps into the field for primary igneous carbonates (Taylor et al., 1967).

Hydrothermal alteration of host and fault rocks

In order to resolve geochemical changes in fault and host rocks during deposition of the VBF hydrothermal mineralisation, we performed lithogeochemical analyses of unaltered host tonalite gneiss and gabbro from footwall domain D. The obtained data were compared with the data gathered from altered host-rock equivalents, including mineralised veins and cataclasites from core zones A1 and A2 (Fig. 5). The litho-geochemical data were used for construction of isocon diagrams (Fig. 18), following the method proposed by Grant (1986). In the diagrams, Al_2O_3 and TiO_2 are considered immobile and are, for each sample, used to delineate a second reference line, which takes into account apparent depletion of elements in the host rock when injected by hydrothermal quartz and calcite veins.

Separate isocon diagrams are constructed for the alteration of host-rock tonalite gneiss (Fig. 18A) and gabbro (Fig. 18B), respectively. For both rock types, similar mobility trends are observed for ore-bearing elements: Zn and Cu are the major metals hydrothermally added to the system, together with minor amounts of S, Pb, As, Bi, Cd, Li, Ag and trace Sb. On the other hand, the major elements (expressed as oxides) show much larger variations; e.g., Na_2O is depleted in both of the altered host rocks of core zones A1 and A2, relative to unaltered host rocks (domain B2), whereas MgO and Fe_2O_3 are enriched. Other oxides like K_2O are slightly depleted in altered tonalite gneiss and enriched in altered gabbro, while MnO shows opposite trends in altered tonalite gneiss vs. gabbro, respectively.

$\delta^{13}C$ and $\delta^{18}O$ stable isotope data

Stable isotope data of calcite from various geological settings on Vanna were analysed, in order to infer potential sources of CO_2. Analysed samples show a wide range of $\delta^{13}C$ and $\delta^{18}O$ isotope values (Fig. 19). The hydrothermal vein calcites from VBF yielded $\delta^{13}C$ values in the range of -5.7 to -4.0‰, and $\delta^{18}O$ values from +7.1 to +12.3‰, overlapping with igneous carbonates (Taylor et al., 1967). In contrast, calcite from the hanging wall, Skipsfjord Nappe (for location see Fig. 5) shows distinctly higher $\delta^{13}C$ (-1 to +5‰) and

$\delta^{18}O$ values (+11 to +16‰) than hydrothermal calcite in the VBF. Calcite samples from veins and breccia in diorite cutting the Vanna Group metasedimentary rocks (see Fig. 3 for location; Bergh et al. 2007) all yielded $\delta^{13}C$ (-4 to +1‰) and $\delta^{18}O$ isotope values (+8 to +12‰), i.e., consistently higher than for the VBF calcites, but lower than for calcites in the Skipsfjord Nappe. By comparison, $\delta^{13}C$ (+1 to +5‰) and $\delta^{18}O$ (+8 to +10‰) values for calcite cement in metasandstones of the Vanna Group (Johannessen, 2012) differ from all the other analysed samples.

Discussion

The data presented above show that the Cu–Zn mineralised zones in the VBF resulted from a multiphase history of fracturing, cataclasis and hydrothermal vein injections into Neoarchaean gneisses as host rocks and the VBF acting as a conduit for the hydrothermal fluids. Mineral chemistry, fluid inclusion micro-thermometry, and stable isotope results were used to gain insight into the ore-forming processes and P-T-X conditions during mineralisation. Based on these data, a tentative paragenetic model is proposed for the Cu–Zn mineralisation in the VBF (Fig. 20), and this model is discussed and argued for below.

Fault-zone architecture, evolution and relationship to Cu–Zn mineralisation

The brittle VBF developed as a normal fault zone affecting Neoarchaean tonalite/gneisses in the footwall wn-faulted Palaeoproterozoic, metasedimentary rocks of the Skipsfjord Nappe/Vanna Group in the hanging wall (Bergh et al., 2007). These basement host rocks comprise a main ductile fabric/foliation which formed in a fold-thrust belt system during the Svecofennian orogeny at greenschist-facies conditions (Bergh et al., 2007). A younger retrogressive, semi-ductile/brittle tectonothermal event produced chlorite shear bands that may record the onset of Palaeozoic (Carboniferous–Permian) brittle faulting along the VBF (cf., Davids et al., 2013).

The brittle VBF is composed of two core zones surrounded by damage zones and undeformed host rocks, with fracture networks cemented by quartz-carbonate veins (Figs. 5 & 6). The structural evolution of the VBF included up to four stages of brittle normal faulting, hydrothermal veining (Figs. 7 & 11), and alteration of the crystalline bedrock (Fig. 12). These events seem to have controlled the Cu–Zn mineralisation (as summarised in Fig. 20B1–B3). To further argue for the evolution and relative timing of textures and veins, the structures are discussed chronologically, in terms of pre-, syn-, or post-tectonic development relative to the ore-forming processes.

The ductile, pre-ore fabrics of the host-rock tonalitic gneisses and quartz-feldspathic schists in the foot-wall and hanging wall of the VBF, respectively, are presumed to be Neoarchaean (c. 2.7 Ga) to Palaeoproterozoic (c. 1.8 Ga) in age (Corfu et al., 2003; Myhre et al., 2013). These host rocks, however, were affected by networks of truncating chlorite-rich shear bands (Fig. 9) that may record the onset of brittle faulting along the VBF.

The initial stages of syn-ore brittle faulting along the VBF generated massive proto/orthocataclasites in core zone A1 along the contact between the host tonalites and gabbroic dykes (Fig. 20A, B1). These cataclasites were enclosed by a matrix of injected quartz-sphalerite (QS) hydrothermal veins, as evidenced by cross-cutting relationships (Figs. 7 & 11H–L). This early process of brittle fracturing and cataclasis may have increased the porosity of the fault rocks and created space for further hydrothermal fluid flow, and thus suggests that the fault core A1 at least initially acted as a fluid conduit. It is, however, reasonable to conclude that during successive injection of QS vein material, this fault core became partly or fully sealed, thus reducing the permeability and forcing the later fluids to flow into the damage zones (cf., Indrevær et al., 2014).

The next stage in the fault evolution was continued cataclasis and injection of quartz- and chalcopyrite-bearing (QCp) veins. This significantly more extensive syn-ore faulting and hydrothermal event produced ultracataclasites and QCp vein breccia infill that post-dated the QS veins in core zone A1. QCp veins represent the first and dominant generation of vein material to be deposited in core zone A2, and also formed as stockwork and sheeted veins in fractures within damage zones B1 and B2 (Fig. 20B2), in close association with secondary chlorite, cookeite and microcline in the matrix of the ultracataclasites.

The presence of multiple generations of cataclasites and Cu–Zn-bearing vein injections, as observed in core zone A2, suggests that the porosity of the fault rocks increased by continued fault movement, and allowed episodic flow of over-pressurised fluids capable of transporting fine-grained, crushed material from elsewhere along the fault. Episodic fluid flow is supported by several phases of injected flow-banded ultra-cataclasites (Fig. 11C, D, J–L) in close spatial relationships to zoned euhedral quartz with plumose textured rims (Fig. 8). The matrix between such zoned quartz grains was filled by new injected cataclasite and QCp veins. This abrupt change in texture from zoned quartz cores, where the rate of deposition is considered slow, to plumose quartz textures at the rims, indicating a faster rate of silica deposition, may have been caused by a change in pressure from lithostatic to hydrostatic due to fracturing along the fault (Fournier & Potter, 1982; Dong et al., 1995; Rimstidt, 1997). This process with cyclic opening of a fault due to over-pressured fluids is known as seismic pumping (Sibson et al., 1975).

The last main syn-tectonic hydrothermal events (stages iii) affecting the VBF included infill of calcite in QS and QCp veins, growth of calcite as the main gangue mineral in the late, cross-cutting barren veins in all fault domains (Ca veins), and possibly also formation of sphalerite-calcite breccias near the rim of core zone A1, although timing of the latter is uncertain. However, textural observations suggest that sphalerite was deposited as part of the early QS vein phase, subsequently brecciated and cemented by latest-stage calcite (see Fig. 11B).

Post-ore brittle fault movements along the VBF generated unconsolidated fault gauge (Fig. 10B) which is observed along the contact with Skipsfjord Nappe rocks, thus separating the Cu–Zn mineralised fault core-damage zones from the non-mineralised hanging wall (Fig. 20B3).

Our data show that the VBF acted as a fluid conduit infiltrating permeable fault rocks with reduced host-rock strength during several stages (i–iv) of brittle fracturing and cataclasis. The mapped VBF architecture, and close relation of microtextures and accumulated ore-forming hydrothermal veins confirms that Cu–Zn mineralisation was controlled by evolution of the fault rocks. The VBF also clearly must have acted, at least intermittently and locally, as a barrier that helped localisation and enrichment of Cu–Zn mineralisation. Fluids migrating in the crust may effectively reduce the strength of the rock by increasing the pore pressure and decreasing the frictional resistance (Hubbert & Rubey, 1959; Sibson et al., 1975). Changes in pore pressure and frictional characteristics may have occurred along the VBF. For example, the pore pressure may have approached lithostatic values during the syn-ore forming hydrothermal events (Figs. 20A, B), as inferred from: (i) growth of euhedral zoned quartz on fracture surfaces, and (ii) injections of multiple generations of flow-banded ultracataclasites, likely from reworked fault core rocks. One requirement for fluids to hold fractures open allowing euhedral quartz growth is a pore pressure that at least exceeds the confining pressure (Hubbert & Rubey, 1959). Conversely, if over-pressurized fluids injected the fault zone, such fluids may have contributed to enhance faulting and further evolution of the fault architecture itself. Therefore, we favour a model involving a successive and/or repeated supply of over-pressurised hydrothermal fluids, from a variety of sources (Fig. 20C), in a tectonic environment characterised by crustal extension and normal faulting (cf., Indrevær et al., 2013, 2014) to explain the complex Cu–Zn mineralisation in the VBF.

P-T-X conditions

Temperature constraints during brittle faulting and injection of Cu–Zn-bearing hydrothermal veins are indicated from chlorite geochemistry and by microthemometric measurements of primary fluid inclusions. Homogenisation temperatures measured from spahlerite-hosted inclusions range from 164 to 218°C, and represent the minimum fluid temperature for the ore-bearing fluids during the first mineralisation phases. Combining this data with chlorite geochemistry that indicate formation temperatures of 280–305°C ± 30°C, does provide some additional constraints. However, chlorite geochemistry is extremely sensitive to later overprints and temperature estimates should be treated with care (Vidal et al., 2006). This is exemplified by the prograde overprint shown in Fig. 13B (Table 2) where a c. 20°C increase from core to rim is suggested, likely as a result of seismic pumping allowing fluxes of hotter ore-bearing fluids to penetrate through the fault.

Ideally, formation pressures could be constrained from isochores constructed based on microthermometric measurements of fluid inclusions combined with temperature estimates from chlorite geothermometry. However, the steepness of isochores from these highly saline (and dense) fluids, combined with the rather large temperature range (including uncertainties) in the chlorite geothermometric estimates cannot provide adequate constraints on the pressure/depth of ore formation. Previous work from Indrevær (2014) who studied several onshore Late Permian normal faults of the Vestfjord–Vanna fault complex in western Troms, containing hydrothermal quartz and K-feldspar, yielded minimum P-T conditions of 300–275°C and 2.4–2.2 kbar. The temperature range overlap with that estimated from VBF, and we cautiously suggest that similar PT conditions could be used for VBF.

Fluid inclusion data and microthermometric measurements suggest that the ore--bearing fluid is composed of H_2O–NaCl–$CaCl_2$ with a general NaCl/$CaCl_2$ ratio of c. 0.3 (Table 2). Regardless of the uncertainties in the accuracy of the salinity calculations, the various calculations show that the fluids are highly saline (20–37 wt.% NaCl + $CaCl_2$). Analyses of evaporate mounds also suggested two different fluid compositions: one fluid with a significant proportion of sulphur, and one without. In addition, isocon diagrams suggest that sulphur was added to the mineralising system, and we therefore suggest that the ore-bearing fluid also contained sulphur. In addition to sulphur and the ore-forming metals Zn and Cu, the isocon diagrams suggest that the ore-bearing fluid likely also contained (or remobilised) minor amounts of metals including Pb, As, Bi, Cd, Li and Ag (Fig. 18).

Redox potential of ore-bearing fluids

As suggested above, the ore-bearing fluids at the VBF contain sulphur (Figs. 16 & 17), but the speciation of sulphur is not known, and depends on whether the fluids have reducing or oxidising properties. According to Zhong et al. (2015), given a high salinity fluid (>22.6 wt.% NaCl) sulphur would be present as sulphate (SO_4^{2-}) in an oxidising fluid, and as H_2S in a reducing fluid.

At the VBF, the alteration of host-rock ilmentite to pyrite (Fig. 12), and general abundance of sulphide ore minerals suggests that these minerals were formed under near neutral pH and reducing conditions, further implying that the ore-bearing fluids were reducing. However, fluids circulating in the upper crust with low water/rock ratios are commonly, at least in part, rock-buffered with sulphate as a common component produced from oxidation of accessory sulphide minerals present in the basement (Bucher & Stober, 2010). In addition, sulphate is identified from the evaporate mounds (Figs. 16 & 17); this sulphate could have formed in two ways, either it was already present in an oxidising ore-forming fluid, or the sulphur was oxidised to sulphate during the decrepitation process when exposed to atmospheric oxygen.

Two equations below exemplify the two potential fluids (reducing fluid in Equation 1 and oxidising fluid in Equation 2). In Equation 1, zinc is carried as a chloride complex in a reducing fluid and sulphur is present in the form of H_2S. The presence of H_2S in the fluid will destabilise the chloride complex carrying the zinc and significantly reduce the solubility of Zn (by shifting the equation to the right). However, higher salinities will

increase the amount of H_2S the fluid can carry without precipitating sphalerite. Reversely, by diluting the fluid the decreasing Cl^- content will shift the equilibrium to the right, and sphalerite will precipitate.

$$ZnCl_{2(aq.)} + H_2S_{(aq.)} = ZnS_{(s)} + 2Cl^- + 2H^+ \quad (1)$$

$$ZnCl_{2(aq.)} + SO_4^{2-} + CH_4 = ZnS_{(s)} + CO_{2(aq.)} + 2Cl^- + 2H_2O \quad (2)$$

Equation 2 describes an oxidising fluid that contains Zn as a chloride complex and sulphur as sulphate (SO_4^{2-}). However, to deposit sphalerite (ZnS) a reducing agent is needed, in this equation exemplified by CH_4. A reducing agent in this type of geological environment could be organic matter; however, no evidence for such matter is found.

Ore-forming processes

Physicochemical properties of fluids control transport and deposition of metals in hydrothermal systems. In the upper crust these fluids are commonly, at least in part, rock-buffered. As a result of these buffering processes, the range in pH and oxygen fugacity of the fluid is relatively narrow and the major controls on metal solubility are temperature and concentration of ligands like chloride and sulphur (Yardley, 2005; Zhong et al., 2015). At the VBF, the ore-bearing fluids have a near neutral pH, have a salinity of c. 27–36 wt.% NaCl + $CaCl_2$, and a temperature estimated in the range of c. 250–335°C. The progressive enrichment of Zn in QS veins (first) followed by Cu in QCp veins (second), and the possible depositional mechanisms for each of these metals will be discussed below.

Zinc and copper in a highly saline fluid at a temperature of c. 300°C are likely transported as chloride complexs, regardless of the oxidation state of the fluid (Zhong et al., 2015). The positive correlation between T_h and salinity from fluid inclusions in sphalerite and in associated QS vein quartz (Fig. 15B) indicate mixing with a colder and less saline fluid, possibly originating as groundwater (Table 2). Mixing and dilution of the fluid would efficiently precipitate sphalerite.

The progressive widening of the fault and repeated injections of fluid through the fault (and deposition of injected cataclasites) are associated with QCp vein deposition. Seismic pumping could lead to an increase in fluid flow, and also to a further influx of a colder and slightly less saline fluid. Such a process is supported by the salinity decrease observed in fluid inclusions from QS to QCp veins. It is further supported by the significant temperature decrease recorded in primary fluid inclusions in QCP vein quartz, and pseudo-secondary inclusions in QS veins (Fig. 15B). It is likely that some of the solid material in the Type 2b fluid inclusions may have been accidentally entrapped microscopic minerals, like chlorite and microcline, from the material that deposited injected cataclasites.

A second contribution to the deposition of chalcopyrite is suggested by textural relationships; chalcopyrite has grown as a rim around clasts, or at the inner edges of the QCp veins, in direct contact with Fe-rich chlorite or pyrite, or chlorite-bearing cataclasite. This suggests that Fe was sourced locally from the host rocks, while sulphurould have been sourced from the hydrothermal fluid (Fig. 17), and that chalcopyrite deposition was enhanced by wall-rock interactions. Wall-rock interactions as a source of Fe may also explain why chalcopyrite mineralisation is chiefly deposited in fractures hosted by mafic (Fe-rich) dyke host rocks (domain B2) and in fault cores of domains A1–A2 with chlorite (Fe-) rich injected ultracataclasites.

Stable isotopic composition of vein-forming fluids

The stable isotope data for hydrothermal calcite from the VBF (Fig. 19) yielded $\delta^{13}C$ values in the range of -5.7 to -4.0‰, and $\delta^{18}O$ values from +7.1 to +12.3‰, which plot close to that of igneous carbonates (Taylor et al., 1967). In general, alteration of igneous carbonate by oxygen-rich atmosphere (e.g., weathering) may cause an increase in the value of $\delta^{18}O$ at a fairly constant $^{13}C/^{12}C$ ratio (Taylor et al., 1967), and such a trend

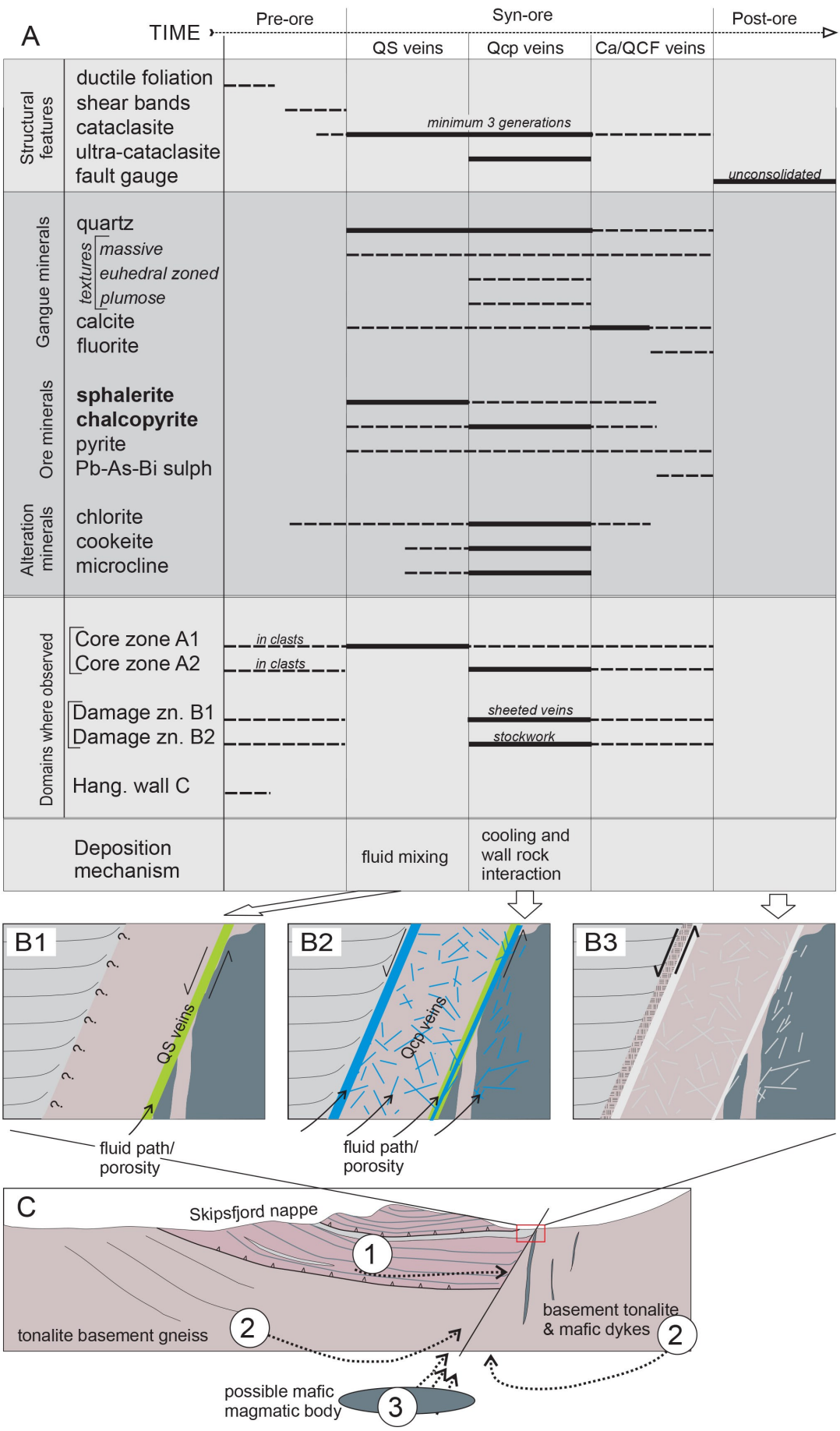
A
TIME
Pre-ore
Syn-ore
Post-ore
QS veins
Qcp veins
Ca/QCF veins
Structural features
ductile foliation
shear bands
cataclasite
ultra-cataclasite
fault gauge
minimum 3 generations
unconsolidated
Gangue minerals
quartz
textures
massive
euhedral zoned
plumose
calcite
fluorite
Ore minerals
sphalerite
chalcopyrite
pyrite
Pb-As-Bi sulph
Alteration minerals
chlorite
cookeite
microcline
Domains where observed
Core zone A1
Core zone A2
in clasts
in clasts
Damage zn. B1
Damage zn. B2
sheeted veins
stockwork
Hang. wall C
Deposition mechanism
fluid mixing
cooling and wall rock interaction
B1
QS veins
B2
Qcp veins
B3
fluid path/ porosity
fluid path/ porosity
C
Skipsfjord nappe
1
2
tonalite basement gneiss
basement tonalite & mafic dykes
2
possible mafic magmatic body
3

Figure 20. Tentative paragenetic evolution model for the VBF and its Cu–Zn mineralisation: (A) Summary of interpreted ore and gangue mineral growth in fault rocks and veins relative to the ore-forming events (pre-, syn-, post-), as seen within textural domains of the VBF. (B) Schematic illustration of the movement and mineralisation history of the VBF, creating porosity and permeability contrasts that may have controlled the injection of QS and QCp veins, and final, post-ore movement (fault gouge). (B1) The early movement caused fracturing, cataclasis and increased permeability in the core zone (domain A1), which acted as a fluid conduit for later injections and cataclasis. (B2) Reduced permeability forced later injections of QCp and Ca-veins into the damage zone and core zone (domain A2). (B3) the final post-ore fault movement generated unconsolidated fault gouge in core zone A2. (C) Schematic representation of possible hydrothermal fluid sources of the mineralised VBF, including; the basinal brines from the cover-basement sequence represented by the meta-sedimentary Skipsfjord Nappe rocks and its lower contact with basement tonalite gneisses (1), the tonalite basement gneisses and enclosed mafic dykes (2), and a possible mafic intrusion (dyke swarm) and/or deep magmatic source (3).

is apparent for hydrothermal calcite associated with the VBF (Fig. 19). Alternatively, the large spread in $\delta^{18}O$ values for the VBF calcite may reflect fluid mixing in the hydrothermal system (Savard & Kontak, 1995; Kontak et al., 2006) and/or assimilation with sedimentary carbonates, as inferred from a pronounced increase of $\delta^{13}C$ in calcite veins of the diorite and matrix of the Vanna Group sedimentary rocks (Fig. 19). The narrow compositional range of $\delta^{13}C$ for VBF calcite, however, strongly supports a magmatic origin of CO_2, and also suggests that factors such as boiling, temperature and oxidation state of the hydrothermal fluid did not influence the $\delta^{13}C$ signature (Rye & Ohmoto, 1974). The fact that calcite from veins in the Skipsfjord Nappe and Vanna Group sedimentary rocks display much higher values of $\delta^{13}C$ and $\delta^{18}O$, larger composiional variations, and more variable trends than calcite in the VBF (Fig. 19) suggests a different origin, and/or possibly a more diverse enrichment history of these carbonates.

Potential origin of the ore-forming fluids

Fluids of the composition described above may have been sourced from several possible hydrological reservoirs, including sediment-derived or shallow-marine brines and entrapped formation water, brine fluids from deeper in the crust, or magmatic and hydrothermal fluids (Yardley, 2005). At Vanna, the relict sedimentary formations are represented by the Palaeoproterozoic Vanna Group rocks deposited in a shallow-marine environment (Binns et al., 1980; Bergh et al., 2007; Johannessen, 2012) and portions of the Skipsfjord Nappe (Opheim & Andresen, 1989), in the hanging wall of the VBF. Deeper brine sources may include the metamorphic tonalitic gneiss and mafic dyke host rocks, or alternatively, magmatic fluids released from a hot magma and transported through faults, fractures and/or along lithological contacts as pathways, and final emplacement in e.g., major faults/shear zones (Fig. 20C).

The role of basinal brines as ore-forming fluids has been widely discussed (Yardley, 2005) and two main models are suggested for their formation (Walter et al., 2016). In the first model, low salinity fluids circulating in the crust are modified by wall-rock interactions and enriched in solutes through hydrothermal alteration of, e.g., feldspar and mica to clay. This model is questioned from experiments by Burisch et al. (2016), indicating that wall-rock interactions are not sufficient to produce brines over 28 wt.% salinities, and therefore, an additional source is required for highly saline fluids. The second model poses an external source of salinity, for example, dissolution of previously deposited evaporates in a sedimentary rock sequence (Mississippi Valley Type deposits; Kesler et al., 1995), or the development and downward migration of so-called bittern brines, a residual brine produced by the precipitation of halite in shallow-marine basins. This process is suggested for the formation of the continental basement brines at Schwarzwald (Walter et al., 2016). Although no evaporates have been observed within the relict shallow-water sedimentary sequences at Vanna, it is not unlikely that at least some of the salinity in the ore-

forming fluid could have been derived from this sequence. However, the $\delta^{13}C$ vs. $\delta^{18}O$ values of VBF calcite veins are distinctly different from those of the Skipsfjord Nappe and Vanna Group (Fig. 19), suggesting that a different source of CO_2 formed these carbonates.

Low Na/Ca ratios, like those at the VBF, have been accredited to fluid-rock interactions by several workers. Banks et al. (1991) suggested a strong host-rock control causing the fluid evolving to a lower Na/Ca ratio for brines analysed in the Central Pyrenees; Boiron et al. (2010) also suggested brine $CaCl_2$-enrichment caused by albitisation and Na-metasomatism, while Bucher & Stober (2010) show that brines may vary from NaCl-rich when residing in granites to $CaCl_2$-rich in mafic rocks like amphibolites and gabbros.

From the discussion above, a possible model for the Cu-Zn-bearing fluid source in the VBF is that the first phase of fluids, associated with QS veins, originated as continent-internal basinal brines with Zn sourced mainly from the surrounding host rocks, possibly with some salinity derived from the meta-sedimentary sequence within the Skipsfjord Nappe. During continental rifting, the increasing amount of Cu associated with the second vein phase (QCp veins) was derived from either a Permian-aged hot mafic melt/dyke (see discussion below), or in combination with wall-rock interactions of a mafic component within the Neoarchaean host-rock gneisses. A magmatic source for the CO_2 in the temporal late hydrothermal calcite veins (Ca veins) is suggested by the low $\delta^{13}C$ and $\delta^{18}O$ values (Fig. 19), indicating that the later fluids included some magmatic CO_2, possibly relating to Permian rift-related magmatism.

Regional implications

A Palaeozoic (348–284 Ma) age of fault rocks along the VBF is well constrained from recent K–Ar dating of illite in late-stage fault gouge (Davids et al., 2013). Such an age contrasts with previous workers arguing for a Palaeoproterozoic VMS stringer zone origin of the Cu–Zn mineralisation, linked with the 2.4 Ga mafic dyke swarm (Ojala et al., 2013; Monsen, 2014) and a subsequent spread of metals into sediments now present in the Skipsfjord Nappe (Opheim & Andresen, 1989). The K-Ar dating results are consistent with formation of the VBF and enclosed Cu–Zn mineralised fault rocks/veins as part of an Early Permian rifting event in the North Norwegian continental margin producing NE–SW striking brittle normal faults and associated fracture sets (Gabrielsen et al., 1990; Faleide et al., 2008; Smelror et al., 2009; Hansen et al., 2012), which later on evolved to major fault zones like the Vestfjord–Vanna and Troms–Finnmark fault complexes (Olesen et al., 1997; Indrevær et al., 2013, 2014; Koehl et al., 2018b). Most of these Permian faults, including the VBF, contain features that indicate complex fluid flow and fault-rock interactions; however, very few of them seem to be accompanied by ore mineralisation (cf., Koehl, 2013; Indrevær et al., 2014).

The wide K–Ar illite age range obtained for the VBF (Davids et al., 2013) could reflect a multiphase kinematic and very complex reactivation history of the fault rocks, as outlined in this work. If a minimum Early Permian age is linked to our post-ore movement unconsolidated fault gauge, the main fault zone movement may have initiated as early as in the Carboniferous, even Late Devonian (cf., Koehl et al., 2018b). Carboniferous rifting is known to have produced mafic dyke swarms on the Finnmark portion of the North Norwegian margin (Roberts et al., 2003; Roberts, 2011; Nasuti et al., 2015) and numerous brittle normal faults with extensive hydrothermal alteration and cataclasis (Indrevær et al., 2013, 2014; Koehl et al., 2018a, b). Specifically, the Langfjorden–Vargsundet fault zone, which can be traced from Troms all along the coast of western Finnmark northward to Magerøya (Fig. 1), experienced multiphase movement and hydrothermal activity (Indrevær et al., 2013, 2014; Koehl et al., 2018a, b). In this fault zone, early-stage quartz- calcite- and laumontite-rich cataclasites initiated at a temperature of about 350–200°C and depth of 2–8 km, and were followed by a main, second period of faulting in the Mid Permian (315–265 Ma) that exhumed basement rocks to shallow depths of 1–3.5 km (Koehl et al., 2018b). Similar results were obtained from several onshore Late Permian normal faults of the Vestfjord–Vanna fault complex in western Troms yielding minimum P-T conditions of 300–275°C and 2.4–2.2 kbar (Indrevær et al., 2014).

These temperature estimates, as discussed above for PT conditions at the VBF (this work) are altogether similar to those of the VBF, i.e., temperatures of 250–335°C. Based on the nature of the brittle faulting and the similar P-T conditions it is therefore likely that the hydrothermal Cu–Zn mineralisation in the VBF was concurrent with the Carboniferous–Permian brittle extensional events that involved multiple brittle faulting, cataclasis and hydrothermal Cu–Zn mineralisation, coupled with a complex reactivation and exhumation history for the faults (cf., Davids et al., 2013).

Regarding a possible magmatic source for some of the hydrothermal fluids in the VBF (see Fig. 20C), no direct evidence of a corresponding hot Permian magmatic and/or volcanic source/dyke for the fluids in the VBF has yet been observed on the Vanna island of western Troms. An exception is a lamproite dyke on Kvaløya farther south, which yielded a Nd- and Sr-isotope age of c. 333 Ma (Kullerud et al., 2011). Extensive rift-related mafic dyke and sill intrusions of Carboniferous–Permian age, however, do exist along the margins of the northern Atlantic Ocean (Kirstein et al., 2006), and also are recorded along portions of the Norwegian continental margin, including northern Finnmark (Lippard & Prestvik, 1997; Roberts et al., 2003; Roberts, 2011; Rice et al., 2014; Nasuti et al., 2015). Thus, and since an increased geothermal gradient exceeding more than 50°C km^{-1} often accompanies incipient continental rifting events, we cannot rule out the possibility that a hidden subsurface, Carboniferous–Permian mafic magma source for hydrothermal Cu–Zn-bearing fluids in the VBF may exist.

Conclusions

1) The Cu–Zn mineralisation in the brittle, late Palaeozoic Vannareid–Burøysund fault on the island of Vanna, West Troms Basement Complex, is hydrothermal, epigenetic and localised within major core and damage zones, suggesting a strong structural (fault) control on the mineralisation.

2) The brittle fault movement and cataclasis of the VBF created porosity allowing fluid flow and deposition of hydrothermal veins and Cu–Zn mineralisation in the core and damage zones, possibly during two main stages of faulting/fracturing. Although the fault cores acted as the main fluid conduits, the fluids also weakened the strength of the fault damage zones and contributed to the complex fault architecture and development history.

3) A paragenetic model is developed for the successive deposition of i) quartz-sphalerite veins, ii) quartz-chalcopyrite veins and iii) calcite veins. Quartz-sphalerite veins were deposited first in the core zone in conjunction with early brittle fracturing and cataclasis, increasing the porosity of the fault rocks and creating space for further hydrothermal fluid flow, confirming that the fault core at least initially acted as a fluid conduit. With further fault movement and widening of the fault, quartz-chalcopyrite veins were deposited in the fault core and damage zones. During successive injection of quartz-sphalerite vein material, the initial fault core became partly or fully sealed, thus reducing the permeability and forcing the later fluids to flow into the damage zones (cf., Indrevær et al., 2014).

4) The hydrothermal ore-bearing fluids in the VBF indicate temperature conditions of c. 250–335°C. Microtextural observations, including injected ultracataclasites, strongly indicate repeated phases of dilation, infill and sealing of the fault. Such seismic pumping processes therefore indicate that the pressure conditions changed repeatedly between lithostatic and hydrostatic end-member values. Similar fault-rock textures are documented from other Permian faults in the West Troms Basement Complex (Indrevær et al., 2014).

5) Ore-forming fluids were near neutral, highly saline (c. 27–36 wt.% NaCl + $CaCl_2$) and composed of H_2O–NaCl–$CaCl_2$ ± S. A fluid with this high salinity is capable of transporting both Cu and Zn as chloride complexes. The ore-bearing fluid was likely a basinal brine with Zn sourced from tonalite gneiss host rocks. Sphalerite was deposited by fluid mixing with a colder and less saline fluid.

Chalcopyrite in QCp veins deposited after sphalerite, likely by a combination of fluid mixing and wall-rock interactions. The stable isotope composition of calcite indicates a magmatic source for the CO_2, and suggests a later magmatic fluid influx, a common feature during continental extension/ rifting.

6) The VBF comprises illite-bearing fault gouge yielding a Palaeozoic (Carboniferous) K–Ar age, thus linking the VBF to a period of incipient extensional faulting and rift basin formation in the Norwegian–Greenland–Barents Sea. Several other faults in the West Troms Basement Complex are related to these early rifting events.

7) This study demonstrates that hydrothermal Cu–Zn mineralisation in northern Norway may occur not only in old Precambrian and Caledonian basement rocks (Sandstad et al., 2015) but also in much younger, Palaeozoic to Cretaceous (?), rift-related, brittle fault zones, and thus provides an additional mineral exploration model for structurally controlled ore deposits.

Acknowledgements. Tobias Bauer and Kristian Drivenes are kindly thanked for reviewing this manuscript. This work was funded by UiT—the Arctic University of Norway. We thank Øystein Rushfeld for access to assay data. Andrea Čobić with the University of Zagreb is thanked for XRD analyses. Kai Neufeld at UiT is acknowledged for his aid and input with SEM analyses. We also acknowledge Mattheus Lindgren at the Centre for Arctic Gas Hydrate, Environment and Climate at UiT for preforming stable isotope analyses.

References

Armitage, P.E.B. & Bergh, S.G. 2005: Structural development of the Mjelde–Skorelvvatn Zone on Kvaløya, Troms: a metasupracrustal shear belt in the Precambrian West Troms Basement Complex, North Norway. *Norwegian Journal of Geology 85*, 117–133.

Augland, L.E., Andresen, A., Gasser, D. & Steltenpohl, M.G. 2014: Early Ordovician to Silurian evolution of exotic terranes in the Scandinavian Caledonides of the Ofoten–Troms area - terrane characterization and correlation based on new U–Pb zircon ages and Lu–Hf isotopes. *In* Corfu, F., Gasser, D. & Chew, D.M. (eds.): *New perspectives on the Caledonides of Scandinavia and related areas,* The Geological Society of London, Special Publications 390, pp. 655–678. https://doi.org/10.1144/SP390.19.

Banks, D.A., Davies, G.R., Yardley, B.W.D., McCaig, A.M. & Grant, N.T. 1991: The chemistry of brines from an Alpine thrust system in the Central Pyrenees: An application of fluid inclusion analysis to the study of fluid behaviour in orogenesis. *Geochimica et Cosmochimica acta 55*, 1021–1030. https://doi.org/10.1016/0016-7037(91)90160-7.

Bergh, S.G., Kullerud, K., Corfu, F., Armitage, P.E.B., Davidsen, B., Johansen, H.W., Pettersen, T. & Knudsen, S. 2007: Low-grade sedimentary rocks on Vanna, North Norway: a new occurrence of a Palaeoproterozoic (2.4–2.2 Ga) cover succession in northern Fennoscandia. *Norwegian Journal of Geology 87*, 301–318.

Bergh, S.G., Kullerud, K., Armitage, P.E.B., Zwaan, K.B., Corfu, F., Ravna, E.J.K. & Myhre, P.I. 2010: Neoarchean to Svecofennian tectono-magmatic evolution of the West Troms Basement Complex, North Norway. *Norwegian Journal of Geology 90*, 21–48.

Binns, R.E., Chroston, P.N. & Matthews, D.W. 1980: Low-grade sediments on Precambrian Gneiss on Vanna, Troms, Northern Norway. *Geological Survey of Norway Bulletin 359*, 61–72.

Blystad, P., Brekke, H., Farsæth, R.B., Larsen, B.T., Skogseid, J. & Tørudbakken, B. 1995: Structural elements of the Norwegian continental shelf. Part II: the Norwegian Sea Region. *Norwegian Petroleum Directorate Bulletin 8*, 1–45.

Bodnar, R.J. & Vityk, M.O. 1994: Interpretation of microthermometric data for H_2O–NaCl fluid inclusions. *In* De Vivo, B. & Frezzotti, M.L. (eds.): *Fluid inclusions in minerals, methods and applications*, Virginia Tech, Blacksburg, VA, pp. 117–130.

Boiron, M.C., Cathelineau, M. & Richard, A. 2010: Fluid flow and metal deposition near basement/cover unconformity: lessons and analogies from Pb–Zn–F–Ba systems for the understanding of Proterozoic U deposits. *Geofluids 10*, 270–292. https://doi.org/10.1002/9781444394900.ch19.

Braathen, A. & Davidsen, B. 2000: Structure and stratigraphy of the Palaeoproterozoic Karasjok Greenstone Belt, north Norway - regional implications. *Norwegian Journal of Geology 80*, 33–50. https://doi.org/10.1080/002919600750042663.

Bucher, K. & Stober, I. 2010: Fluids in the upper continental crust. *Geofluids 10*, 241–253. https://doi.org/10.1002/9781444394900.ch17.

Burisch, M., Marks, M.A.W., Nowak, M. & Markl, G. 2016: The effect of temperature and cataclastic deformation on the composition of upper crustal fluids - an experimental approach. *Chemical Geology 433*, 24–35. https://doi.org/10.1016/j.chemgeo.2016.03.031.

Cathelineau, M. 1988: Cation site occupancy in chlorites and illites as a function of temperature. *Clay Minerals 23*, 471–485. https://doi.org/10.1180/claymin.1988.023.4.13.

Chu, H., Chi, G. & Chou, I.M. 2016: Freezing and melting behaviors of H_2O–NaCl–$CaCl_2$ solutions in fused silica capillaries and glass-sandwiched films: implications for fluid inclusion studies. *Geofluids 16*, 518–532. https://doi.org/10.1111/gfl.12173.

Corbett, G.J. & Leach, T.M. 1998: *Southwest Pacific Rim gold-copper systems; structure, alteration, and mineralization.* Society of Economic Geology Special Publications, 236 pp.

Corfu, F., Armitage, P.E.B., Kullerud, K. & Bergh, S.G. 2003: Preliminary U–Pb geochronology in the West Troms Basement Complex, north Norway: Archean and Palaeoproterozoic events and younger overprints. *Geological Survey of Norway Bulletin 441*, 61–72.

Dallmeyer, R.D. 1992: $^{40}Ar/^{39}Ar$ mineral ages within the Western Gneiss Terrane, Troms: evidence of polyphase Proterozoic tectonothermal activity (Svecokarelian and Sveconorwegian). *Precambrian Research 57*, 195–206. https://doi.org/10.1016/0301-9268(92)90002-6.

Davids, C., Wemmer, K., Zwingmann, H., Kohlmann, F., Jacobs, J. & Bergh, S.G. 2013: K–Ar illite and apatite fission track constraints on brittle faulting and the evolution of the northern Norwegian passive margin. *Tectonophysics 608*, 196–211. https://doi.org/10.1016/j.tecto.2013.09.035.

Davids, C., Benowitz, J.A., Layer, P.W. & Bergh, S.G. 2018: Direct $^{40}Ar/^{39}Ar$ K-feldspar dating of Late Permian-Early Triassic brittle faulting in northern Norway. *Terra Nova 30*, 263–269. https://doi.org/10.1111/ter.12333.

Dong, G., Morrison, G. & Jaireth, S. 1995: Quartz textures in epithermal veins, Queensland - classification, origin, and implication. *Economic Geology* 90, 1841–1856. https://doi.org/10.2113/gsecongeo.90.6.1841.

Dubois, M., Monnin, C., Castelain, T., Coquinot, Y., Gouy, S., Gauthier, A. & Goffè, B. 2010: Investigations of the H_2O–NaCl–LiCl system: a synthethic fluid inclusion study and thermodynamic modeling from -50° to +100°C and up to 12 mol/kg. *Economic Geology 105*, 329–338. https://doi.org/10.2113/gsecongeo.105.2.329.

Eilu, P., Hallberg, A., Bergman, T., Feoktistov, V., Korsakova, M., Krasotkin, S., Kuosmanen, E., Livineko, V., Nurmi, P.A., Often, M., Philippov, N., Sandstad, J.S., Stromov, V. & Tontti, M. 2008: Metallic mineral deposit map of the Fennoscandian Shield, scale 1:2,000,000, *Geological Survey of Finland, Geological Survey of Norway, Geological Survey of Sweden & The Federal Agency of use of mineral resources of the Ministry of Natural Resources of the Russian Federation*.

Faleide, J.I., Tsikalas, F., Breivik, A.J., Mjelde, R., Ritzmann, O., Engen, Ø., Wilson, J. & Eldholm, O. 2008: Structure and evolution of the continental margin off Norway and the Barents Sea. *Episodes 31*, 82–91. https://doi.org/10.18814/epiiugs/2008/v31i1/012.

Forslund, T. 1988: *Post-kaledonske forkastninger i Vest-Troms: med vekt på Straumsbukta-Kvaløyslettaforkastningen, Kvaløya*. MSc thesis, UiT The Arctic University of Tromsø, 160 pp.

Fournier, R.O. & Potter, R.W. 1982: An equation correlating the solubility of quartz in water from 25° to 900°C at pressures up to 10,000 bars. *Geochimica et Cosmochimica acta 46*, 1969–1973. https://doi.org/10.1016/0016-7037(82)90135-1.

Franklin, J.M., Lydon, J.W. & Sangster, D.F. 1981: Volcanic-associated massive sulfide deposits. *In* Skinner, B.J. (ed.): *Economic Geology 75th Anniversary Volume 75*, pp. 485–627.

Gabrielsen, R.H. & Braathen, A. 2014: Models of fracture lineaments - joint swarms, fracture corridors and faults in crystalline rocks, and their genetic relations. *Tectonophysics 628*, 26–45.

Gabrielsen, R.H., Farsæth, R.B., Jensen, L.N., Kalheim, J.E. & Riis, F. 1990: Structural elements of the Norwegian continental shelf - Part I: the Barents Sea Region. *Norwegian Petroleum Directorate Bulletin 6*. https://doi.org/10.1016/j.tecto.2014.04.022.

Galley, A.G., Hannington, M. & Jonasson, I. 2007: Volcanogenic massive sulphide deposits. *In* Goodfellow, W.D. (ed.): *Mineral deposits of Canada: a synthesis of major deposit-types, district metallogeny, the evolution of geological provinces, and exploration method*, Geological Association of Canada, Mineral deposits division, pp. 141–161.

Grant, J.A. 1986: The isocon diagram - a simple solution to Gresens' equation for metasomatic alteration. *Economic Geology 81*, 1976–1981. https://doi.org/10.2113/gsecongeo.81.8.1976.

Griffin, B.J., Joy, D.C. & Michael, J.R. 2010: A comparison of a luminescence –based VPSE and an electron based GSED for SE and CL imaging in variable pressure SEM with conventional SE imaging. *Microscopy and Microanalysis 16*, 624–625. https://doi.org/10.1017/S1431927610058691.

Haaland, L.C. 2018: *Geometry and kinematic evolution of ductile shear zones in the Ersfjord Granite (1.79 Ga), West Troms Basement Complex: a Svecofennian accretionary thrust system*. MSc thesis, Department of Geosciences, UiT The Arctic University of Norway, Tromsø, 79 pp.

Hansen, J.A., Bergh, S.G. & Henningsen, T. 2012: Mesozoic rifting and basin evolution on the Lofoten and Vesterålen margin, North Norway; time constraints and regional implications. *Norwegian Journal of Geology 91*, 203–228.

Hemley, J.J. & Cygan, C.L. 1992: Hydrothermal ore-forming processes in the light of studies in rock-buffered systems: iron-copper-zinc-lead sulfide solubility relations. *Economic Geology 87*, 1–22. https://doi.org/10.2113/gsecongeo.87.1.1.

Hubbert, M.K. & Rubey, W.W. 1959: Role of fluid pressure in mechanics of overthrust faulting. *Bulletin of the Geological Society of America 70*, 115–166. https://doi.org/10.1130/0016-7606(1959)70[115:ROFPIM]2.0.CO;2.

Indrevær, K., Bergh, S.G., Koehl, J.B., Hansen, J.A., Schermer, E.R. & Ingebrigtsen, A. 2013: Post-Caledonian brittle fault zones on the hyperextended SW Barents Sea margin: New insights into onshore and offshore margin architecture. *Norwegian Journal of Geology 93*, 167–189.

Indrevær, K., Stunitz, H. & Bergh, S.G. 2014: On Palaeozoic-Mesozoic brittle normal faults along the SW Barents Sea margin: fault processes and implications for basement permeability and margin evolution. *Journal of the Geological Society of London 171*, 831–846. https://doi.org/10.1144/jgs2014-018.

Ingebritsen, S.E. & Manning, C.E. 2010: Permeability of the continental crust: dynamic variations inferred from seismicity and metamorphism. *Geofluids 10*, 193–206. https://doi.org/10.1111/j.1468-8123.2010.00278.x.

Johannessen, H. 2012: *Tinnvatnformasjonen i Vannas proterozoiske lagrekke: Sedimentære facies og avsetningsmiljø*. MSc thesis, Department of Geology, University of Tromsø, 105 pp.

Johansen, H. 1987*: Forholdet mellom det prekambriske underlaget og overliggende sedimentære bergarter sør-øst på Vanna, Troms*. MSc thesis, Institutt for biologi og geologi. Universitetet i Tromsø, 136 pp.

Kesler, S.E., Appold, M.S., Martini, A.M., Walter, L.M., Huston, T.J. & Kyle, J.R. 1995: Na–Cl–Br systematics of mineralizing brines in Mississippi Valley-type deposits. *Geology 23*, 641–644. https://doi.org/10.1130/0091-7613(1995)023<0641:NCBSOM>2.3.CO;2.

Kirstein, L.A., Davies, G.R. & Heeremans, M. 2006: The petrogenesis of Carboniferous–Permian dyke and sill intrusions across northern Europe. *Contributions to Mineralogy and Petrology 152*, 721–742. https://doi.org/10.1007/s00410-006-0129-9.

Koehl, J.B. 2013: *Late Paleozoic-Cenozoic fault correlation and characterization of fault rocks in western Troms, North Norway.* PhD thesis, Department of Geology, UiT The Arctic University of Norway, 108 pp.

Koehl, J.B., Bergh, S.G., Henningsen, T. & Faleide, J.I. 2018a: Middle to Late Devonian–Carboniferous collapse basins on the Finnmark Platform and in the southwesternmost Nordkapp basin, SW Barents Sea. *Solid Earth 9*, 341–362. https://doi.org/10.5194/se-9-341-2018.

Koehl, J.B., Bergh, S.G., Osmundsen, P.T., Redfield, T.F., Indrevær, K., Lea, H. & Bergø, E. 2018b: Late Devonian–Carboniferous faulting in NW Finmark and controlling fabrics. *Norwegian Journal of Geology 99*, 1–40. https://doi.org/10.17850/njg99-3-5.

Koistinen, T., Stephens, M.B., Bogatchev, V., Nordgulen, Ø., Wennerström, M. & Korhonen, J. 2001: Geological map of the Fennoscandian Shield, scale 1:2,000,000, *Geological surveys of Finland, Norway, Sweden, and the north-west department of ministry of Natural Resources of Russia.*

Kontak, D.J. 2004: Analysis of evaporate mounds as a complement to fluid-inclusion thermometric data: case studies from granitic environments in Nova Scotia and Peru. *The Canadian Mineralogist 42*, 1315–1330. https://doi.org/10.2113/gscanmin.42.5.1315.

Kontak, D.J., Kyser, K., Gize, A. & Marshall, D. 2006: Structurally controlled vein barite mineralization in the Maritimes Basin of eastern Canada: geologic setting, stable isotopes, and fluid inclusions. *Economic Geology 101*, 407–430. https://doi.org/10.2113/gsecongeo.101.2.407.

Kucha, H. & Pawlikoswki, M. 1986: Two-brine model of the genesis of strata-bound Zechstain deposits (Kupferschiefer type), Poland. *Mineralium Deposita 21*, 70–80. https://doi.org/10.1007/BF00204365.

Kullerud, K., Skjerlie, K.P., Corfu, F. & de la Rosa, J.D. 2006: The 2.40 Ga Ringvassøy mafic dykes, West Troms Basement Complex, Norway: The concluding act of early Palaeoproterozoic continental breakup. *Precambrian Research 150*, 183–200. https://doi.org/10.1016/j.precamres.2006.08.003.

Kullerud, K., Zozulya, D., Bergh, S.G., Hansen, H. & Ravna, E.J.K. 2011: Geochemistry and tectonic setting of a lamproite dyke in Kvaløya, North Norway. *Lithos 126*, 278–189. https://doi.org/10.1016/j.lithos.2011.08.002.

Lippard, S.J. & Prestvik, T. 1997: Carboniferous dolerite dykes on Magerøy; new age determinations and tectonic significance. *Norwegian Journal of Geology 77*, 159–163.

Meinert, L.D., Dipple, G.M. & Nicolescu, S. 2005: World skarn deposits. *In* Hedenquist, J.W., Thompson, J.F.H., Goldfarb, R.J. & Richards, J.P. (eds.): *One hundred anniversary volume*, Society of Economic Geology 100, pp. 299–336. https://doi.org/10.5382/AV100.11.

Monsen, K. 2014: *Hydrothermal Cu–Zn mineralization at Vanna, West Troms Basement Complex*. MSc thesis, Department of Geology, UiT The Arctic University of Norway, 109 pp.

Mosar, J. 2003: Scandinavias North Atlantic passive margin. *Journal of geophysical research 108*, 2360–2377. https://doi.org/10.1029/2002JB002134.

Mosar, J., Eide, E.A., Osmundsen, P.T., Sommaruga, A. & Torsvik, T. 2002: Greenland–Norway separation: a geodynamic model for the North Atlantic. *Norwegian Journal of Geology 82*, 281–298.

Myhre, P.I., Corfu, F. & Bergh, S.G. 2011: Palaeoproterozoic (2.0–1.95 Ga) pre-orogenic supracrustal sequences in the West Troms Basement Complex, North Norway. *Precambrian Research 186*, 89–100. https://doi.org/10.1016/j.precamres.2011.01.003.

Myhre, P.I., Corfu, F., Bergh, S.G. & Kullerud, K. 2013: U–Pb geochronology along an Archean geotransect in the West Troms Basement Complex, North Norway. *Norwegian Journal of Geology 93*, 1–24.

Nasuti, A., Roberts, D. & Gernigon, L. 2015: Multiphase mafic dykes in the Caledonides of northern Finnmark revealed by a new high-resolution aeromagnetic dataset. *Norwegian Journal of Geology 95*, 285–298. https://doi.org/10.17850/njg95-3-02.

Ojala, J.V., Hansen, H. & Ahola, H. 2013: Cu–Zn mineralisation at Vannareid, West Troms Basement Complex: a new Palaeoproterozoic VMS occurrence in the northern Fennoscandian Shield. *Abstracts and proceedings, 12th Biennial SGA Meeting, 12–15 August, Uppsala, Sweden,* p. 2.

Olesen, O., Torsvik, T.H., Tveten, E., Zwaan, K.B., Løseth, H. & Henningsen, T. 1997: Basement structure of the continental margin in the Lofoten–Lopphavet area, northern Norway: Constraints from potential field data, on-land structural mapping and palaeomagnetic data. *Norwegian Journal of Geology 77*, 15–30.

Olesen, O., Lundin, E., Nordgulen, Ø., Osmundsen, P.T., Skilbrei, J.R., Smethurst, M.A., Solli, A., Bugge, T. & Fichler, C. 2002: Bridging the gap between the onshore and offshore geology in Nordland, northern Norway. *Norwegian Journal of Geology 82*, 243–262.

Opheim, J.A. & Andresen, A. 1989: Basement-cover relationships on northern Vanna, Troms, Norway. *Norwegian Journal of Geology 69*, 67–81.

Oszczepalski, S. 1999: Origin of the Kupferschiefer polymetallic mineralization in Poland. *Mineralium Deposita 34*, 599–613. https://doi.org/10.1007/s001260050222.

Perelló, J., Clifford, J.A., Creaser, R.A. & Valencia, V.A. 2015: An example of synorogenic sediment-hosted copper mineralization: geologic and geochronologic evidence from the Paleoproterozoic Nussir Deposit, Finnmark, arctic Norway. *Economic Geology 110*, 677–689. https://doi.org/10.2113/econgeo.110.3.677.

Rice, A.H.N. 1990: A discussion: Basement-cover relationships on northern Vanna, Troms, Norway. *Norwegian Journal of Geology 70*, 179–186.

Rice, A.H.N. 2014: Restoration of the External Caledonides, Finnmark, North Norway. *Geological Society of London Special Publication 390*, 271–299. https://doi.org/10.1144/SP390.18.

Rimstidt, D.J. 1997: Gangue mineral transport and deposition. *In* Barnes, H.L. (ed.): *Geochemistry of hydrothermal ore deposits*, 3rd edition, John Wiley & Sons Inc, New York, pp. 487–515.

Roberts, D. 2011: Age of the Hamningberg dolerite dyke, Varanger Peninsula, Finnmark: Devonian rather than Vendian - a revised interpretation. *Geological Survey of Norway Bulletin 451*, 32–36.

Roberts, D. & Lippard, S.J. 2005: Inferred Mesozoic faulting in Finnmark: current status and offshore links. *Geological Survey of Norway Bulletin 443*, 55–60.

Roberts, D., Torsvik, T., Andersen, T.B. & Rehnström, E.F. 2003: The Early Carboniferous Magerøy dykes, northern Norway; palaeomagnetism and palaeogeography. *Geological Magazine 140*, 443–451. https://doi.org/10.1017/S0016756803008082.

Roedder, E. 1984: *Fluid inclusions*. U.S. Geological Survey, Blacksburg, Virginia, 644 pp. https://doi.org/10.1515/9781501508271.

Rye, R.O. & Ohmoto, H. 1974: Sulfur and Carbon isotopes and ore genesis: a review. *Economic Geology 69*, 825–843. https://doi.org/10.2113/gsecongeo.69.6.826.

Sandstad, J.S. 2015: MINN - mineral resources in North Norway. *Norwegian Journal of Geology 95,* 211–216.

Savard, M.M. & Kontak, D.J. 1995: $\delta^{13}C$–$\delta^{18}O$–$^{87}Sr/^{86}Sr$ covariations in ore-stage calcites at and around the Gays River Zn–Pb deposit (Nova Scotia, Canada) - evidence for fluid mixing. *Economic Geology 93*, 181–196. https://doi.org/10.2113/gsecongeo.93.6.818.

Schmid, S.M. & Handy, M.R. 1991: Towards a genetic classification of fault rocks: geological usage and tectonophysical implications. *In* Muller, D.W., McKenzie, J.A. & Weissert, H. (eds.): *Controversies in modern geology*, Academic press, London, pp. 339–361.

Seward, T.M. & Barnes, H.L. 1997: Metal transport by hydrothermal ore fluids. *In* Barnes, H.L. (ed.): *Geochemistry of hydrothermal ore deposits*, 3rd edition, John Wiley & Sons Inc, New York, pp. 435–486.

Sheperd, T.J. 1985: *A practical guide to fluid inclusions*. Blackie & Son Ltd, Glasgow, 235 pp.

Sibson, R.H. 1977: Fault rocks and fault mechanisms. *Journal of the Geological Society of London 133*, 191–216. https://doi.org/10.1144/gsjgs.133.3.0191.

Sibson, R.H., Moore, J.M. & Rankin, A.H. 1975: Seismic pumping - a hydrothermal fluid transport mechanism. *Journal of the Geological Society of London 131*, 653–659. https://doi.org/10.1144/gsjgs.131.6.0653.

Simmons, S.F., White, N.C. & John, D.A. 2005: Geological characteristics of epithermal precious and base metal deposits. *In* Hedenquist, J.W., Thompson, J.F.H., Goldfarb, R.J. & Richards, J.P. (eds.): *One hundred year anniversary volume*, Society of Economic Geology 100, pp. 485–522. https://doi.org/10.5382/AV100.16.

Smelror, M., Petrov, O., Larssen, G.B. & Werner, S. 2009: *Geological history of the Barents Sea*. Geological Survey of Norway, 135 pp.

Steele-MacInnis, M., Bodnar, R.J. & Naden, J. 2011: Numerical model to determine the composition of H_2O–NaCl–$CaCl_2$ fluid inclusions based on microthermometric and microanalytical data. *Geochimica et Cosmochimica acta 75*, 21–40. https://doi.org/10.1016/j.gca.2010.10.002.

Taylor, H.P., Frechen, J. & Degens, E.T. 1967: Oxygen and carbon isotope studies of carbonatites from the Laacher See District, West Germany and the Alnö District, Sweden. *Geochimica et Cosmochimica acta 31*, 407–430. https://doi.org/10.1016/0016-7037(67)90051-8.

Thorstensen, L. 2011: *Land-sokkel korrelasjon av tektoniske elementer i ytre del av Senja og Kvaløya i Troms*. MSc thesis, Department of Geology, University of Tromsø, 117 pp.

Vanko, D.A., Bodnar, R.J. & Sterner, S.M. 1988: Synthetic fluid inclusions: VIII. Vapor-saturated halite solubility in part of the system NaClCaC12-H20, with application to fluid inclusions from oceanic hydro-thermal. *Geochimica et Cosmochimica acta 52*, 2451–2456. https://doi.org/10.1016/0016-7037(88)90303-1.

Vaughan, D.J. & Craig, J.R. 1997: Sulphide ore stabilities, morphologies, and intergrowth textures. *In* Barnes, H.L. (ed.): *Geochemistry of hydrothermal ore deposits*, 3rd edition, John Wiley & Sons Inc, New York, pp. 367–434.

Vidal, O., De Andrade, V., Lewin, E., Munoz, M., Parra, T. & Pascarelli, S. 2006: P-T-deformation-Fe^{3+}/Fe^{2+} mapping at the thin section scale and comparison with XANES mapping: application to a garnet-bearing metapelite from the Sambagawa metamorphic belt (Japan). *Journal of Metamorphic Geology 24*, 669–683. https://doi.org/10.1111/j.1525-1314.2006.00661.x.

Walter, B., Burisch, M. & Markl, G. 2016: Long-term chemical evolution and modification of continental basement brines - a field study from the Schwarzwald, SW Germany. *Geofluids 16*, 604–624. https://doi.org/10.1111/gfl.12167.

Wilkinson, J.J. 2001: Fluid inclusions in hydrothermal ore deposits. *Lithos 55*, 229–272.

Wise, D.U., Dunn, D.E., Engelder, J.T., Geiser, P.A., Hatcher, R.D., Kish, S.A., Odom, A.L. & Schamel, S. 1984: Fault-related rocks: Suggestions for terminology. *Geology 12*, 391–394. https://doi.org/10.1130/0091-7613(1984)12<391:FRSFT>2.0.CO;2.

Yardley, B.W.D. 2005: Metal concentrations in crustal fluids and their relationship to ore formation. *Economic Geology 100*, 613–632. https://doi.org/10.2113/100.4.613.

Zhong, R., Brugger, J., Chen, Y. & Li, W. 2015: Contrasting regimes of Cu, Zn and Pb transport in ore-forming hydrothermal fluids. *Chemical Geology 395*, 154–164. https://doi.org/10.1016/j.chemgeo.2014.12.008.

View publication stats